The final publication is available at Elsevier via https://dx.doi.org/10.1016/j.msea.2018.04.020 © 2018. This manuscript version is made available under the CC-BY-NC-ND 4.0 license https://creativecommons.org/licenses/by-nc-nd/4.0/

Author's Accepted Manuscript

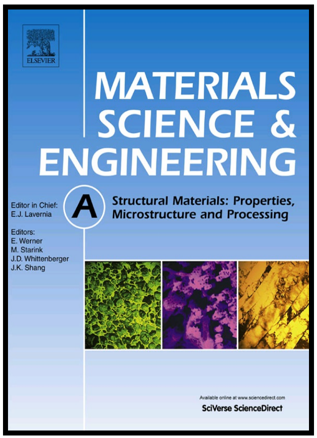

www.elsevier.com/locate/msea

A New Crystal Plasticity Framework to Simulate the Large Strain Behavior of Aluminum Alloys at Warm Temperatures

Edward D. Cyr, Abhijit Brahme, Mohsen Mohammadi, Raja K. Mishra, Kaan Inal

PII: S0921-5093(18)30517-3
DOI: https://doi.org/10.1016/j.msea.2018.04.020
Reference: MSA36340

To appear in: *Materials Science & Engineering A*

Received date: 6 June 2017
Revised date: 5 April 2018
Accepted date: 6 April 2018

Cite this article as: Edward D. Cyr, Abhijit Brahme, Mohsen Mohammadi, Raja K. Mishra and Kaan Inal, A New Crystal Plasticity Framework to Simulate the Large Strain Behavior of Aluminum Alloys at Warm Temperatures, *Materials Science & Engineering A,* https://doi.org/10.1016/j.msea.2018.04.020

This is a PDF file of an unedited manuscript that has been accepted for publication. As a service to our customers we are providing this early version of the manuscript. The manuscript will undergo copyediting, typesetting, and review of the resulting galley proof before it is published in its final citable form. Please note that during the production process errors may be discovered which could affect the content, and all legal disclaimers that apply to the journal pertain.

A New Crystal Plasticity Framework to Simulate the Large Strain Behavior of Aluminum Alloys at Warm Temperatures

Edward D. Cyr[1], Abhijit Brahme[1], Mohsen Mohammadi[2], Raja K. Mishra[3], Kaan Inal[1]

[1]*Department of Mechanical and Mechatronics Engineering, University of Waterloo, Waterloo ON, Canada, N2L 3G1*
[2]*Department of Mechanical Engineering, University of New Brunswick, Fredericton NB, Canada,*
[3]*General Motors Research & Development Center, Warren MI, 48090, USA*

Abstract

To improve metal formability, high temperature forming has become a desired manufacturing process. Phenomenological plasticity models are widely used in this application, however lack good predictive capability concerning microstructure evolution during forming. Many crystal plasticity hardening models have been developed to predict deformation phenomena of metals during high temperature forming; however, few have thermodynamic self-hardening formulations based on deformation mechanisms. This work presents a crystal plasticity based analysis with a Taylor polycrystal averaging scheme of warm forming employing a new microstructure and dislocation based strain hardening model to simulate deformation behaviour. The hardening model is derived from energy balance between dislocation storage, dislocation accumulation, and dislocation recovery, based on remobilization of immobile dislocations, due to thermal activation. The constitutive formulation is extended to include alloying effects due to solute strengthening of Mg. The material hardening properties of AA5754 are characterized for a range of temperatures at constant strain-rates. A formulation for the kinematics of dynamic strain aging is presented and employed for room-temperature simulations. The hardening characterization is then used to predict stress-strain behaviour of AA5182 for similar conditions. The model shows excellent predictability of experimental results. An analysis on the microstructural connection between temperature and stress-strain response is presented.

Keywords: Crystal Plasticity; Dislocation; Recovery; Temperature; Aluminum; Texture.

1. Introduction

For decades, mass reduction has been a priority in the automotive sector for improving fuel economy (Greene & DiCicco, 2000). Many manufacturers have opted for substituting typical steel components for lighter aluminum alloys. An application of particular interest in this study is the use of 5xxx series aluminum-magnesium sheet alloys in panel components. The difficulty with aluminum sheet, in the replacement of panel components, is the lower formability at room temperatures than in steels (Ayres & Wenner, 1979). In addition, surface quality of formed parts at room temperature is undesirable due to the Lüder's lines and serrated flow behaviour of Al-Mg sheet alloys (dynamic strain aging/PLC effect) (Robinson & Shaw, 1994). However, poor formability and surface finish can be greatly improved by warm forming (Li & Ghosh, 2003) without expensive production costs of refining microstructure to achieve the same outcome. Hot deformation processing is a desirable method for shaping in industry due to the ability to refine microstructure, which significantly influences the mechanical response and can increase formability (Zhang et al., 2004; Li, et al., 2011). Elevated temperature forming corresponds to a decreased flow stress and increased ductility of the sheet, which can allow deep drawing and stretch in panels competitive with steels without design modifications. The understanding of high temperature deformation behaviour for warm forming and the constitutive relations describing the material flow are two of the fundamental prerequisites for the advancement of forming technology in industry.

Dynamic softening mechanisms, such as dynamic recovery (DRV) often occur in aluminum alloys with high-stacking fault energies during deformation at elevated temperatures. Numerous reports on the high-temperature deformation behaviour and dynamic softening of aluminum alloys (and other FCC metals) have shown that the mechanisms contributing to softening, recovery, and microstructure evolution during high-temperature deformation are highly sensitive to temperature and strain-rate (Clayton, 2005; Abedrabbro et al., 2007; Pandey et al., 2013; Ezatpour et al., 2014). Determination of the effects of temperature and strain rate on high-temperature deformation in metals has been a topic of discussion for decades (Argon, 1968; Kocks et al., 1975; Kocks, 1976, 2001; Anand, 1982; Mecking et al., 1986; Kocks & Mecking, 2003; Terentyev et al., 2015; Kooiman et al., 2015, 2016). Flow stress is the most basic and useful measure for characterizing plastic deformation properties of metals and provides a means to determine the energy required to plastically deform a metal. The balance between energy storage and plastic strain accommodation by mechanisms of slip-deformation can be evaluated with the aid of governing constitutive equations to provide good predictability. The improvement of these constitutive models over recent decades have given rise to an incredible understanding of material behaviour on a fundamental level; however, in many cases at the expense of great complexity and subsequently increased difficulty in application.

Available research for simulation of warm forming processes focuses only on the effect of elevated temperature on the evolution of the flow stress or hardening (Li & Gosh, 2003; Takata et al., 2000; Naka et al., 2001; Boogaard et al., 2001), rather than the effect of elevated temperature on microstructural parameters that lead to this behaviour. Confidence in numerical analysis of plasticity of materials depends greatly on the accuracy of the constitutive model describing the behaviour of the material (Chung & Shah, 1992). This is of particular importance when the material exhibits anisotropy caused by texture, for example, in rolled sheets. The importance of an appropriate material model for predicting even simple monotonic loading strain paths has been demonstrated (Brahme et al., 2011).

Plasticity theories are widely used in research and industry covering a broad field of applications ranging from crash and extrusion simulations to modeling and optimization of material microstructures. However, empirical phenomenological plasticity theories fail to predict the mechanical behaviour of micro-components and the corresponding material response. The methods of crystal plasticity have been successfully used fill this gap in modeling local non-homogeneous mechanical behaviour, and has been applied extensively to study plastic deformation and texture evolution (Roters et al. 2010). The material hardening, however, is usually empirical, or is based on dislocation models relying on many fitting variables or complex special gradient/misorientation determinations for dislocation density. These models are usually only adequate at ambient temperature up to bulk failure strain deformation. It is essential for the investigation of complex deformation features during forming, such as temperature dependent and geometric softening, strain localization, and microstructure evolution, etc., that the material hardening models are derived from physical deformation mechanics.

Crystal plasticity has been successfully used in modeling non-homogeneous mechanical behaviour and has been applied extensively to study both heterogeneous plastic deformation and texture evolution (Roters et al. 2010). The collectives of crystal plasticity with the finite element method (CPFEM) and Taylor polycrystal analysis have proven a very powerful tool for the investigation of such plastic phenomena as the Bauschinger effect (Kim et al., 2012), formability (Wu et al., 1997; Inal et al., 2005; Mohammadi et al., 2014), cyclic loading (Muhammad et al., 2015; Grilli et al., 2015), surface effects (Rossiter et al., 2013), texture evolution (Popova et al., 2015; Knezevic et al., 2013) and high rate deformation (Clayton, 2005), to list a few. However, little physical information is directly involved in the well-established crystal plasticity hardening models as most hardening laws are empirical fits, or require complex and computationally expensive calculations of strain gradients to predict dislocation contents (Gerken & Dawson, 2008; Elkhodary & Bakr, 2015). Phenomenological models are satisfactory for the intended use of room temperature deformation, but are typically only able to predict material response up to the specimen failure strains. This is exaggerated when these hardening laws are used to predict large deformation at high temperatures. Large strain predictability is essential for the investigation deformation behaviour during forming. The ability to model phenomena such as thermal softening, geometric softening, strain localization, and microstructure evolution, etc., require material hardening models be derived from physical deformation mechanics.

In first part of this study, a physical theory for temperature dependent strain hardening in FCC polycrystals is developed based on dislocation accumulation and recovery. The model is then fit with available pure aluminum uniaxial stress-strain data (Kocks, 1976) and temperature dependent hardening parameters are identified and investigated. Finally, the resulting temperature dependencies and theory are used to predict the stress-strain curves at a new strain rate and a parameter sensitivity analysis is completed. Then the developed model is implemented in a Taylor-type crystal plasticity model to simulate the deformation behaviour of Al-Mg aluminum alloys (AA) 5754 and 5182 at elevated temperatures. The material hardening properties of AA5754 sheet are characterized for a range of temperatures from 25ºC to 260ºC at constant strain rates using experimental data obtained from literature. The available experimental data was reported to be at constant low strain rate such that thermal straining effects can be neglected. A kinematic formulation to capture dynamic strain aging at room temperature is also implemented to accurately represent the temperature dependency of the material hardening. Finally, the hardening characterization is used to predict stress-strain behaviour of AA5182 sheet over the same temperature and strain rate ranges.

2. Temperature Dependent Single Crystal Hardening Model

Work hardening has always been a topic of great interest for scientists and engineers studying plastic deformation in metals. The work-hardening reflects the way in which networks of stored dislocations, both geometrically-necessary and statistically-stored, impede the passage of moving dislocations. Individual dislocations may act as point obstacles causing short-range interactions, or can form junctions. The collective network, a source of long-range internal stresses. Following the discovery of dislocations and dislocation theory, many concentrated efforts by the scientific community led to the description of the three stages of work hardening in single crystals: primary slip (stage I), multiple slip (stage II), and cross slip and recovery (stage III). The first stage is only observed in single crystals at low strain where hardening is governed by statistically-stored dislocations. Although flow stress theory and strain hardening is derived from single crystals, most metals strained in application are polycrystalline, characterized by yield followed by a low-strain high-hardening stage II that transitions, often rapidly, into a lower hardening stage III. The theory on the initiation of stage III began with the work of Seeger and coworkers (Schoeck and Seeger, 1955; Seeger et al., 1959) which begins because cross-slip occurs upon sufficient local pile-up stresses. The model predicts an exponential variation of the onset of stage III with temperature, however, was met with controversy (Coulomb and Friedel, 1957). Much debate exists on the high-strain transition from a stage III to a stage IV hardening, where the stress-strain curve begins to plateau or become nearly linear, however this is typically not observed under uniaxial conditions due to localization.

Single crystal work hardening theories based simply on the concept of hardening stages have been employed in crystal plasticity framework and can successfully be tuned to match the polycrystal behaviour; however, there still exists a significant gap in the connection between physical properties and mechanisms of deformation in explaining work hardening through the use of hardening laws. This is even more obvious at high temperatures, where conventional stage II to stage III transition broadens and the region of the stress-strain curve corresponding to each becomes unclear. In addition, the extremely low stage III hardening relative to the high stage II cannot be predicted with conventional crystal plasticity hardening models. Therefore, a hardening relationship based on the dislocations themselves, rather than the behaviour that manifests as multiple “stages” of hardening, must be developed in order to predict temperature dependent hardening.

The relationship between material strength and the square root of total dislocation density is well known as

$$\sigma = \sigma_0 + M\alpha\mu b\sqrt{\rho} \tag{1}$$

where M is the Taylor factor relating shear and normal stresses in polycrystals ($\sigma = M\tau$), α is a measure of the strengthening effect of dislocations, μ is the shear modulus, and b is Burgers vector (Kuhlmann-Wilsdorf 1970). Initial material strength σ_0 is due greatly to alloying, precipitates, particles, and grain size. The significance of this equation is that all work hardening models from earlier theories attributing work hardening to dislocation pile-ups, tangles, jogs, and forest dislocations and newer statistical theories and models of decreasing mean free path all predict this proportionality of strength and the square root of dislocation density. This equation is also maintained by nearly all experimental results (Rodriguez 1996).

Taylor (1934) proposed that stress to propagate a mobile dislocation could be predicted as the shear stress required to overcome a stable array of immobile (sessile) ±edge dislocations. The calculated stress was dependent on the inter-layer spacing of sessile dislocations. Since the plastic shear strain is related to the motion of dislocation, Taylor's analysis of shear strain found the stress to be proportional to the square root of the strain and exhibited the proportionality as follows

$$\frac{\tau}{\mu\sqrt{\gamma}} = \frac{\kappa\sqrt{b}}{\lambda} \tag{2}$$

here τ and γ are the shear stress and shear strain, respectively, μ is the shear modulus, b is Burgers vector, λ is the mean slip distance, and κ is a proportionality constant related to the sessile dislocation array. Taylor was able to estimate λ using calculated values of κ from modeled dislocation arrays and compared the magnitude with experimental observations (Taylor 1934). In addition, Taylor's model with parabolic stress-strain dependence predicts a constant λ.

More recent work (Saimoto & Van Houtte 2011) has provided evidence that the mean slip distance can be measured directly from the experimental stress-strain curve with a single variable ϕ using the following relation:

$$\lambda = \phi \frac{b}{2} \frac{\mu^2}{\tau} \frac{\partial\gamma}{\partial\tau_{|T,\dot{\gamma}}} \tag{3}$$

Here the hardening term $\partial\tau/\partial\gamma_{|T,\dot{\gamma}}$ is the slope of the shear stress-strain curve, however has previously been estimated as θ_{II} evaluated from a Stage II type hardening determination of [100] single crystals (Nabarro et al. 1964, Saimoto 2006). Consequently, the determination of mean slip distance can be a function of τ or γ. Based on this assumption, the calculation of λ to produce an incremental strain $\Delta\gamma$ is possible.

The Taylor model defines an increment in shear strain $\Delta\gamma$ to be equal to $N\tilde{A}b$, where N is the volume density of slip patches produced by a source of inter-obstacle spacing ℓ on slip patch area $\tilde{A}$. An increase in dislocation length associated with the slipped area arises from the expanding perimeter of the propagating dislocation segment from the source. Dislocation length may also decrease due to annihilation interactions with other existing dislocation segments. The slipped area can be approximated as proportional to the square of the mean slip distance λ^2 assuming that λ is in the order of the average inter-obstacle spacing such that $\lambda \approx \ell$ (assumed at low strains). By Saimoto-Van Houtte analysis (2009), one can describe the incremental change in statistical dislocation density per unit area, $\Delta\rho^{create}$, due to incremental shear strain as follows:

$$\Delta\rho^{create} = \frac{P}{A}\frac{\Delta\gamma}{\lambda b} \tag{4}$$

where P/A is a unit-less parameter for the ratio of the expanding dislocation perimeter P divided by statistical annihilation factor A and is temperature dependent.

An estimation of P is possible through a quantitative analysis of the advance of a dislocation through a random array of obstacles (Friedel, 1964; Foreman and Makin, 1966, 1967; Kocks, 1967; Altintas, 1978). The analysis can be derived from the Altintas (1978) diagram of randomly dispersed point obstacles, shown in Figure 1. The algebraic relationships between the interobstacle spacing $\ell = \ell_s$, dislocation arc radius R, height of new sector h (assumed here that $h = \lambda$, mean slip distance), which are determined by the strength of obstacle parameter such that $\alpha \approx \cos(\psi/2)$. The initial length of the dislocation segment bound by obstacles A and C is equal to $\ell_i = R\sin(\pi-\psi)$ and the final dislocation length $\ell_f = 2R(\pi-\psi)$. The ratio of the increase in dislocation length can therefore be calculated as $(\ell_f - \ell_i)/2\ell_i$. Given $\psi/2 \ = 65^0$ corresponding to $\alpha = 0.4$, P for this analysis is approximately 0.2.

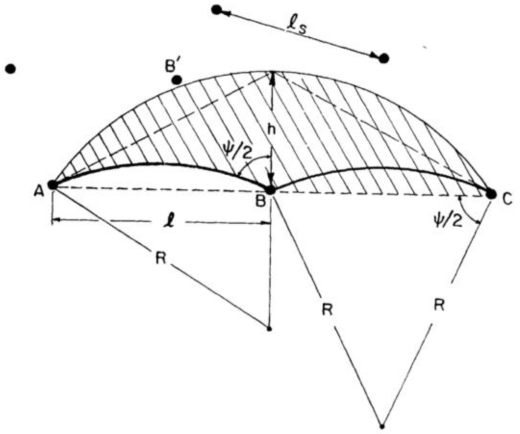

Fig. 1. Geometry of randomly distributed obstacles. (Friedel, 1964).

If we take the well-known relationship in equation (1) between the strength of a polycrystal and the square root of the dislocation density, we can obtain

$$\frac{d\rho}{d\tau} = \frac{2\tau}{(\alpha\mu b)^2} \tag{5}$$

Therefore, for small increments in material strength the required stored dislocation density must be equal to

$$\Delta\rho^{stored} = \frac{2(\tau\Delta\tau)}{(\alpha\mu b)^2} \tag{6}$$

Finally, we can equate the dislocation density stored due to increasing material strength and the dislocation content created necessary to accommodate an incremental shear strain in differential form,

$$\left|\frac{2(2\tau\partial\tau)}{(\alpha\mu b)^2}\right|^{stored} = \left|\frac{P}{A}\frac{\partial\gamma}{\lambda b}\right|^{created} \tag{7}$$

The above relationship represents the condition where dynamic recovery of dislocations due to thermodynamic recovery is not accounted for. The statistical annihilation of dislocation lines $1/A$ accounts for the statistical probability that two oppositely oriented mobile dislocations exist within a threshold proximity on a given slip plane and annihilate nearly instantaneously. This is experimentally very difficult to determine; however, statistical annihilation of new dislocations has been shown to be very important in order to predict the experimental stress-strain curve (Saimoto & Van Houtte, 2011).

In all dislocation models, work hardening is a result of mobile dislocations that produce strain being pinned and therefore unable to exit through a surface, be absorbed by grain boundaries, or annihilating each other. Instead, some fraction of these mobile dislocations are stored in the crystals forming new obstacles to continued slip of other dislocations. As discussed previously, this is represented as the dislocation density created through shear straining, or $\Delta\rho^{created}$. If we now include the mechanisms facilitating recovery, the total change in dislocation density can be represented as follows:

$$d\rho^{stored} = d\rho^{created} - d\rho^{recovered} \tag{8}$$

The first two terms have been described above, while the last term is the change in dislocation density due to recovery or rearrangement of previously stored dislocations. The recovery processes are still not well understood and various mechanisms have been proposed to describe them. The following proposed mechanism for recovery is rationalized from experimental observations in conjunction with accepted theories from dislocation mechanics.

A crystal with potential number of recovery sites in a differential area on a slip plane can be denoted as ρda where ρ is the stored dislocation density. If an average dislocation line length of ℓ_r is recovered or annihilated, the change in total dislocation line length $d\ell$ per volume V is written as

$$\frac{d\ell}{V} = \frac{\ell_r \rho da}{V} = d\rho^{recovered} \tag{9}$$

The importance of this relationship is the understanding that the probability of a dislocation being recovered is directly proportional to the probability that a moving dislocation discovers a recovery site, and therefore the dislocation density itself. This can now be linked to the shear increment by the following equation. Assuming a slip plane area da in a volume V shears a distance of one Burgers vector, the incremental shear can be represented as

$$d\gamma = \frac{bda}{V} \tag{10}$$

Combining the above two equations, the recovered dislocation density can now be written in terms of the shear increment as

$$d\rho^{recovered} = \frac{\ell_r}{b}\rho d\gamma = \Omega \rho d\gamma \tag{11}$$

where Ω is called the recovery factor which represents the average length of dislocation that is recovered normalized by the Burgers vector for a given shear increment. Finally, we combine this with equations (4), (6) and (8) to get the following:

$$\left|\frac{2(2\tau\partial\tau)}{(\alpha\mu b)^2}\right|^{stored} = \left|\frac{P}{A}\frac{\partial\gamma}{\lambda b}\right|^{created} - |\Omega\rho\partial\gamma|^{recovered} \tag{12}$$

By integration, one can write:

$$\left[\frac{2\tau^2}{(\alpha\mu b)^2}\right]_{\tau_1}^{\tau} = \left[\frac{P}{A}\frac{\gamma}{\lambda b} - \Omega\rho\gamma\right]_{\gamma_1}^{\gamma} \tag{13}$$

The difficulty now becomes the determination of dislocation density ρ. This is achieved implicitly by substitution of the Taylor expression from equation (1), which allows for a work hardening plastic flow rule to be developed based on material parameters and internal state variables given by,

$$\tau = \alpha\mu b\sqrt{\frac{P}{A}\frac{\gamma}{\lambda b(2+\Omega\gamma)}} \tag{14}$$

To this point, the work hardening model assumes that the total dislocation density is approximately equal to the statistically stored dislocation density. This assumption is valid if the geometric slip distance λ_g is significantly larger than the slip distance for statistically stored dislocations λ_s. However, according to Ashby (1970), geometrically necessary dislocations begin to dominate if $\lambda_g < \lambda_s$ as measured from the length of the slip lines in work-hardened material. This becomes significant when (i) the recovery of statistically stored dislocations is great enough to increase λ_s approaching λ_g, and (ii) when microstructural effects at higher strains, such as the formation of dislocation cells, reduce λ_g. Using the Ashby approach, whereby it is assumed that the two dislocation densities can be added linearly in stress-strain space, their total contribution to the flow stress is given by the following equation:

$$\tau = \alpha\mu b\sqrt{\rho_s + \rho_g} \tag{15}$$

where

$$\rho_s = \frac{P}{A}\frac{\gamma}{\lambda b(2 + \Omega\gamma)} \tag{16}$$

According to the definition proposed by Ashby (1970), geometric slip distance λ_g is characteristic of the microstructure as well as the type and distribution of hardening precipitates/particles or dislocation impeding structures in the material. Here, λ_g will represent the formation of long-range dislocation structures in the form of cell walls with λ_g related to the size of these cells. From Ashby, the density of geometrically necessary dislocations due to a cellular structure is related to the imposed shear strain and the slip distance λ_g through the relationship given as

$$\rho_g = \frac{\kappa}{b}\frac{\gamma}{\lambda_g} \tag{17}$$

where κ is a proportionality constant related to the microstructure geometry, and type of obstacle (Ashby, 1970).

Finally, the new plastic flow rule follows from the substitution of equations (16) and (17) into (15):

$$\tau = \alpha\mu b\sqrt{\frac{\gamma}{\Lambda_s b(2 + \Omega\gamma)} + \frac{\gamma}{\Lambda_g b}} \tag{18}$$

The capitalized Λ_s and Λ_g are material parameters related to the statistical and geometric slip distances such that $1/\Lambda_s = P/A\lambda_s$ and $1/\Lambda_g = \kappa/\lambda_g$. It is noted that, work hardening does not explicitly account for time-rate dependence; however, this is considered in the determination of the recovery parameter discussed in the following section. The slip distance parameters will also have a rate dependence and a temperature dependence and is discussed in section 3.

2.1 Dynamic Recovery

It has been shown in many studies that FCC metals exhibit dynamic recovery – the dynamic annihilation of dislocations given sufficient dislocation density and thermal energy – at warm temperatures (Hirthe & Lothe, 1967; Kocks, 1976; Gottstein, 2013). The mechanisms of dynamic recovery can be divided into (i) cross-slip and (ii) vacancy climb (Bergström & Hallen, 1982; Hallen, 1985). At low temperatures, well below ambient for aluminum, recovery is assumed to be assisted by the mechanism of cross-slip of screw dislocations. At ambient temperatures and above, the effects of cross-slip become nearly constant and can be considered athermal. However, vacancy climb dominates recovery at higher temperatures. A schematic of the effects of cross-slip and vacancy climb as mechanisms of recovery is presented in Figure 2.

Vacancy climb – or dislocation climb due to vacancy diffusion – may not significantly contribute to the deformation, but is an important mechanism in the recovery process (Kocks, 1976). Therefore, following Figure 2, it is reasonable to assume that dynamic recovery can be decomposed into two components as $\Omega = \Omega_0 + \Omega(\dot{\gamma}, T)$ where Ω_0 is the athermal component and $\Omega(\dot{\gamma}, T)$ symbolizes a dynamic recovery factor dependent on strain rate $\dot{\gamma}$ and temperature T.

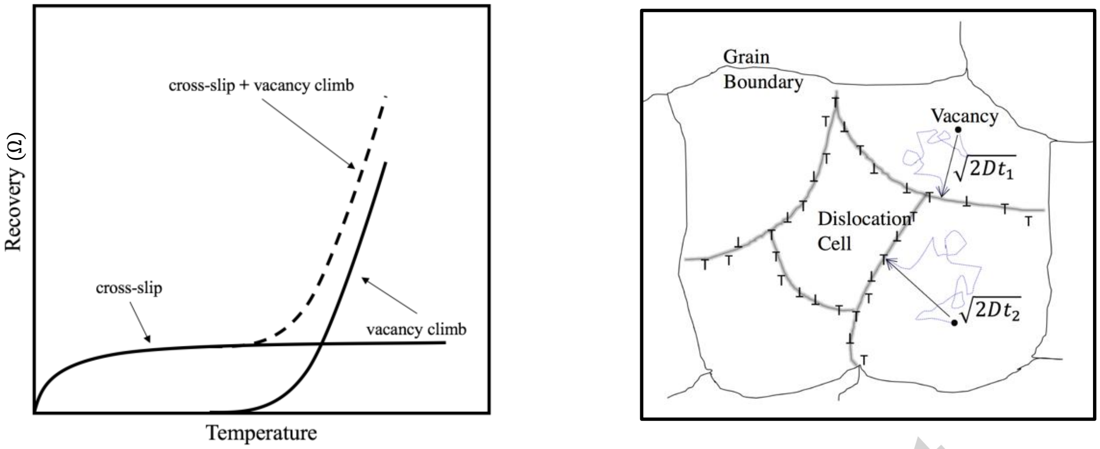

(a) (b)

Fig. 2. (a) A schematic representation of recovery mechanisms in two components, at low temperatures recovery is assisted by cross-slip and at high temperatures recovery is dominated by vacancy climb; (b) and diagram of interior vacancies migrating by the mechanism of random walk and reaching the dislocation cell wall following the Einstein relationship $\delta = \sqrt{2Dt}$.

In order to derive a theoretical expression for this dependence, a few assumptions must be made. Firstly, (i) the remobilization of sessile dislocations occurs primarily at dislocation cell walls where dislocation density is maximum. This is supported by high-powered electron microscopy studies (Bergrstrøm, 1977; Gottstein, 2004; Mompiou et al., 2012). Following this, (ii) the remobilization mechanism is a result of vacancy climb of the sessile dislocations. This is favourable due to the supersaturation of vacancy sites quickly achieved during straining, and the exponential increase in vacancy mobility at elevated temperatures. (iii) During plastic deformation, these vacancies migrate to dislocation cell walls where they are absorbed, facilitating dislocation climb. And lastly, (iv) the diffusion of vacancies is governed by the Einstein relationship $\delta = \sqrt{2Dt}$ where δ is the average distance moved by the vacancies during a time t, and D is the diffusion coefficient. By the assumption of vacancy supersaturation, the diffusion coefficient D can be defined by the Arrhenius relationship $D = D_0 \exp(-Q_m/RT)$ where D_0 is a constant related to entropy of diffusion, Q_m is the energy of vacancy diffusion, R is the gas constant and T is absolute temperature.

Next, we need a relationship for the number of vacancies that will reach the cell walls after some given time t. This must be proportional to the density of vacancies n_0 and the average distance δ a vacancy has migrated after some time. According to the assumptions made previously, the remobilization of sessile dislocations in the cell walls is conducted via vacancy climb, therefore it is reasonable that recovery, or $\Omega(\dot{\gamma}, T)$, is proportional to the number of vacancies reaching the cell walls such that

$$\Omega(\dot{\gamma}, T) = \mathcal{K} n_0 \sqrt{2Dt} \tag{19}$$

with $\mathcal{K}$ representing a proportionality constant related to the geometry of the cellular substructure.

If the average distance a vacancy travels in time t is given by δ, then an average time can be found for a dislocation to travel a distance δ. By differentiation of equation (11) with respect to time and solving for $\rho(t)$, the average wait time can be determined to be equal to $1/\Omega\dot{\gamma}$ (see Appendix A). If we only consider thermal component of the total recovery, then this can be substituted back into equation (19) and rearranged to yield

$$\Omega(\dot{\gamma}, T) = A_0 \left(\frac{D_0}{\dot{\gamma}}\right)^{1/3} \exp\left(-\frac{Q_m}{3RT}\right) \tag{21}$$

where A_0, which is proportional to $\mathcal{K} n_0$, is the only unknown parameter. The values of D_0, Q_m, and R are tabulated data, and temperature and strain rate are from experimental conditions.

2.2 Elevated Temperatures

The measured hardening parameters outlined in the previous section are temperature dependent. It has been shown experimentally that these material properties evolve with temperature, and strain (Niewczas et al., 2015). Foreman and Makin (1966, 1967) completed extensive research on dislocation movement through arrays of obstacles, including the effect of temperature. It was proposed that the stress required to propagate dislocations passed an obstacle decreased at an exponential rate with respect to temperature of the form

$$\left(\frac{\tau}{\tau_0}\right)^{\frac{2}{3}} = 1 - \left(\frac{T}{T_0}\right)^{\frac{p}{p+1}} \tag{22}$$

where τ_0 represents the strength at absolute zero and T_0 represents the temperature at which the stress to overcome an obstacle becomes vanishingly small, and p is a constant. This realization was attributed to the weakening line tension of dislocations; thus, the breaking angle to overcome the obstacle increases. However, the consensus for aluminum has been that the obstacle strength parameter α undergoes negligible change with changing temperature, suggesting that the breaking angle to overcome obstacles is more or less constant (Diak et al. 1998; Saimoto 2006; Park and Niewczas 2008; Niewczas et al. 2015).

More difficult is statistical annihilation parameter and mean slip distance. It seems logical they would evolve with temperature and strain, as provided by equation (3); however, the interdependence of these parameters gives extreme difficulty in understanding the individual temperature and strain dependence. For instance, a variation in λ by fitting the geometric factor ϕ is balanced by P/A (Appendix B), and therefore the product of these terms is a constant. By analysis of equations (3) and (14), $1/\Lambda_s$ is directly proportional to $\tau\theta$ as:

$$\frac{1}{\Lambda_s} = \frac{P}{A}\frac{1}{\lambda} = \frac{4\tau\theta}{(\alpha\mu)^2 b} \tag{23}$$

where the minimum mean slip distance λ_{min} is synonymous with the maximum of the product of the flow stress and strain hardening rate $\tau\theta$, corresponding to parabolic type hardening (see figure 3).

Decades of research have been conducted on the understanding of the behaviour of dislocation propagation and mean slip distance (Taylor 1934; Cottrell and Stokes 1955; Basinski 1959; Foreman and Makin 1967; Louat 1978; Diak et al. 1998; Park and Niewczas 2008; Altintas 2011). What has been concluded is that, upon initial straining λ is nearly equal to the inter-obstacle spacing ℓ and increases during deformation to a length directly related to cell size. This model presents these as Λ_s and Λ_g related to short and long-range slip. The influence of temperature, however, is not well understood in literature.

The overall effect of these parameters, following the assumptions and procedures outlined in Appendix B, can be determined and each hardening parameter can be analyzed with respect to their individual temperature dependencies. The most pertinent is the correct determination of the three hardening parameters Λ_s, Λ_g, and Ω ensuring an accurate depiction of their temperature dependency. The method outlined in the Appendix B ensures that this is accomplished. Therefore, in the following section the model will be used to determine parameters Λ_s, Λ_g, and Ω ranging from -73ºC to 327ºC Kelvin for commercially pure aluminum. Relationships between these parameters are discussed and presented graphically to present the temperature dependencies and the model's predictability.

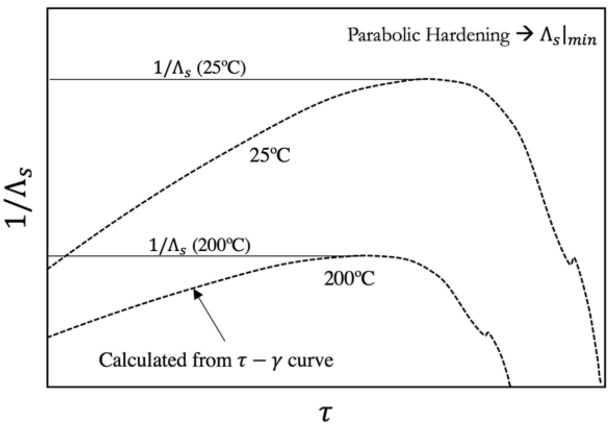

Fig. 3. Determination of $1/\Lambda_s$ from the experimental stress-strain curves is found by plotting equation (23) where the maximum value corresponds to parabolic hardening.

3. Application to Pure Aluminum

The analysis presented in this section is based on stress-strain data of 99.99% pure aluminum polycrystals by uniaxial tension deformation. The obtained experimental results are from the literature (Kocks 1976) for engineering stress and engineering strain in the normal direction and are digitized and converted to true stress and logarithmic strain. The data was then translated to reflect the averages of the shear flow stress τ and shear strain γ of all crystallites in a polycrystal through the Taylor factor. The calibration of simulation parameters, is completed in this section for the pure aluminum at 100ºC temperature intervals between -73ºC and 327ºC. Pure aluminum was chosen due to the availability of data at multiple strain rates as well and the absence of alloying solutes and particles that contribute new hardening effects and can mask the true behaviour of the dislocation-dislocation interactions. In addition, the pure material is free of heat treatable particles, thus the observed thermal effects can be regarded as purely due to the behaviour of the dislocation obstacles and slip dominated deformation. It should also be noted that the grain boundaries will have an effect on the material strength; however, for this study the grain structure is of adequate size to ignore these effects.

3.1 Stress-Strain Calibration

The calibrated hardening parameters at -73ºC to 327ºC are presented in Table 1. The corresponding stress-strain curves are presented in Figure 4 along with the experimental data at a strain rate of $\dot{\varepsilon} = 1/min$. Obstacle strength parameter α is taken from literature data to be equal to 0.4 for all aluminum alloys at room temperature (Saimoto and Van Houtte, 2011) and its temperature dependence is assumed to be negligible in the chosen temperature range, as discussed by Kocks and Mecking (2003). This also corresponds to a constant approximation for $P = 0.2$ (see section 2). The experimental stress-strain data used for commercially pure (99.99%) aluminum is acquired from Kocks (1976).

Table 1. Measured hardening parameters of 99.99% pure aluminum at -73ºC to 327ºC taken at strain rate of $\dot{\varepsilon} = 1/min$. The value for τ_0 was scaled with shear modulus $\mu(T)$ such that τ_0/μ is constant, as determined from Varshni (1970).

Alloy	Temp. *(K)*	α	τ_0 *(MPa)*	Λ_s *(μm)*	Λ_g *(mm)*	Ω
99.99% Pure Aluminum	200	0.4	0.1	14.8	0.450	2.5
	300	0.4	0.1	19.7	0.909	5.5
	400	0.4	0.096	28.3	1.330	11.5
	500	0.4	0.092	43.3	2.38	32.0
	600	0.4	0.087	75.6	15.4	75.0

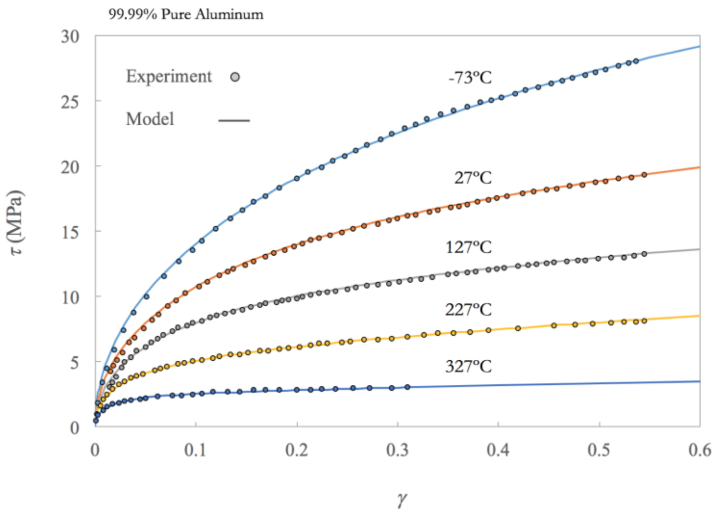

Fig. 4. Experimental (points) and simulated (lines) $\tau - \gamma$ stress-strain curves at -73ºC to 327ºC for commercially pure aluminum $\dot{\varepsilon} = 1/min$. Hardening parameters were determined by the method presented in section 3 and values presented in Table 1.

The model captures the hardening behaviour very well, especially at high strain and high temperatures. At -73ºC, the experimental curve retains a very high hardening below shear strain $\gamma = 0.05$. This could indicate an exaggerated stage II-type hardening prolonged by lack of thermal motivation for stage III. Experimental stress-strain curves for low temperature aluminum presented by Jobba et al. (2015) also show a tendency towards a more linear hardening behaviour as the temperature is decreased below room temperature. This is motivated by two contributing factors: (i) low dislocation density and (ii) low thermal activation for vacancy climb. At sufficiently low temperatures and strain, the material recovery parameter becomes dependent on strain as well as temperature and strain-rate. Upon adequate dislocation accumulation, the dependency falls solely on temperature and strain rate. Near and above room temperature this is not observed, likely due to the added thermal energy facilitating the onset of dynamic recovery at very low strains.

3.2 Dynamic Recovery

The expression dynamic recovery generally refers to a stage III process where there is a decrease in the hardening rate that is strongly dependent on temperature and strain rate. Presented in Figure 5 is the recovery factor Ω at the five fitted temperatures. To determine the value of material parameter A_0 from equation (21), these values are plotted vs. the exponential of the energy term, with $Q_m = 17{,}000\ cal \cdot mol^{-1}K^{-1}$ as provided by Hallén (1985) to provide a linear relationship with slope equal to $A_0(D_0/\dot{\varepsilon})^{1/3}$ and intercept Ω_0. Here, the applied strain rate $\dot{\varepsilon}$ has been used for simplicity and it is assumed to be directly proportional to the shear strain rate by the Taylor factor.

The recovery parameters follow a very clear exponential relationship with material constants determined from a linear fit of Figure 5. The units for A_0 are determined from analysis of equation (21) and are related to the density of vacancies; thus, the recovery parameter Ω is a unit-less parameter. The value plotted for -73ºC is representative of the low temperature recovery mechanism of cross-slip as discussed in Section 2.1. It is clear from the model that at this temperature, the thermal activation of the cross-slip mechanisms has a leading role in the recovery process, and recovery due to vacancy climb is nearly negligible. The dynamic recovery model presented does not consider the low temperature effect of cross-slip but assumes it to be a constant Ω_0. At temperatures below zero centigrade (for aluminum) the athermal Ω_0 becomes temperature dependent; however, Hallén (1985) showed experimentally that this effect is not observed in aluminum until below approximately 200K. Therefore, it is assumed that Ω_0 can be determined as the recovery factor measured at -73ºC.

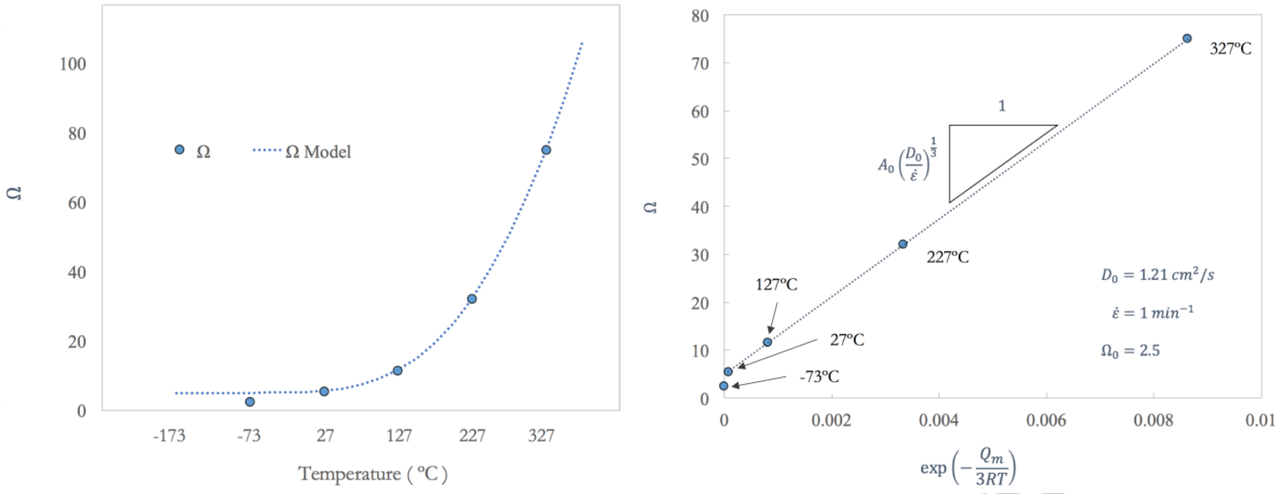

Fig. 5. Presents (left) the dynamic recovery factor Ω vs. temperature for pure aluminum and equation (21) with parameters determined from fitting in (right), the dynamic recovery factor Ω plotted against $\exp(-Q_m/3RT)$ with, A_0 and Ω_0 determined from the linear fit.

Even if the model does not define the spatial distribution of dislocations, our physical picture that during straining dislocations are accumulated by storage processes in randomly distributed webs is very successful at predicting the data. The results presented are quite promising and show that a model for vacancy climb as the dominant mechanism for dynamic recovery is valid for a wide temperature range. This is important in predicting temperature dependent behaviour and ultimately warm forming behaviour where the material strength is significantly affected by material temperature and strain-rate.

3.3 Mean Slip Distance

For this study, the temperature dependence of the geometric-necessary and statistically-stored slip distance parameters Λ_g and Λ_s were investigated graphically. Systematically it was found that a linear relationship with temperature could be drawn with the inverse square-root of the slip distance parameter for statistically-stored dislocations, and the inverse of the slip distance parameter for the geometrically-necessary dislocation density. The difference in these dependencies is not known; however, it is suggested by the results that parameter Λ_s is related to the area swept by the statistically-stored dislocations. This would then allow the proposal that both types of dislocation slip distances, Λ_g and $\sqrt{\Lambda_s}$ hold the same inverse temperature dependencies. Figure 6 demonstrates this relationship, where the inverse of mean slip distance for both types decreases with increasing temperature. However, the value at -73ºC does not necessarily follow this pattern. At -73ºC, the steep increase in $1/\Lambda_g$ alludes to a mechanism activation point, having significant effect on the geometric necessary dislocations. This along with the presented findings for the dynamic recovery factor enhances the notion that different mechanisms inhibit the plastic flow below some low threshold temperature. Due to the relative magnitudes of the slip-distance parameters, the mean slip distance of geometric dislocations begins to dominate the behaviour below room temperature, and this is shown as the rapid decrease in the geometric slip-distance parameter in Figure 6. If the temperature increases above 327ºC, the model predicts that the geometric slip-distance parameter is infinitely large, which seems unrealistic unless this extreme growth in Λ_g represents a complete instability in the cellular substructure. In other terms, upon sufficient thermal energy, cell structures may no longer be stable or their wall unable to impede further propagation of moving dislocations. These predictions correspond with the so called "hot deformation" regime, where new mechanisms become prevalent, such as dynamic recrystallization.

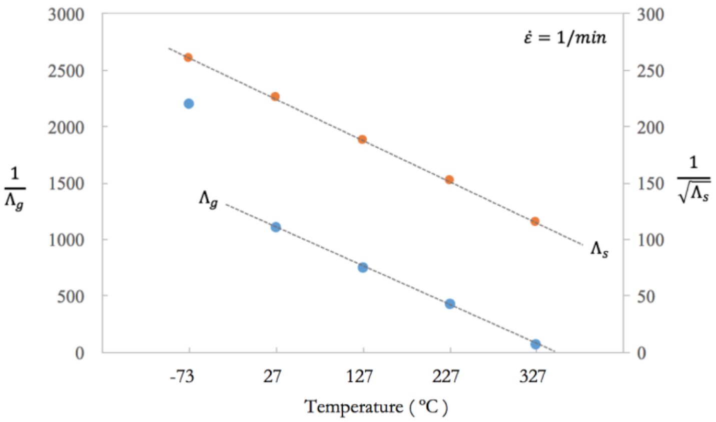

Fig. 6. The linear dependencies of mean slip distance parameter and temperature at $\dot{\varepsilon} = 1/min$ are shown with blue Λ_g and orange Λ_s points representing the values determined from fitted data. The dotted lines highlight the linearity of the inverse square root of Λ_s and the inverse of Λ_g relationships with temperature.

It appears logical that a greater temperature dependency exists on the movement of statistically-stored dislocations. They are greatly affected by recovery, which is a thermodynamically motivated mechanism; and, from dislocation theory, are also dependent on the geometrically-necessary dislocation density (Ashby, 1970). However, the exact temperature dependence of mean free path of any type of dislocation is absent from the literature. There are many contributions to understanding and modeling dislocation mechanics with respect to microstructure and strain rate for a wide veriety of metals and alloys (Svendsen, 2002; Mianroodi et al., 2016; Terentyev et al., 2015), but the effect of temperature and thermal contributions directly affecting the movement, storage, and recovery in strain hardening has not been addressed. Even the descriptions of thermally activated glide of dislocations by Orowan (1940) and dislocation activation area by Kocks et al. (1975) along with the most widely accepted phenomenological description of thermally activated flow and strain hardening (Kocks and Mecking, 2003) do not present any findings or empirical theories on the activation of the slip distance with temperature. Therefore, only speculation on the mechanisms involved in these temperature dependencies can be made here.

Another interesting outcome of this model, is the ability to study the interdependence of these internal variables. The most useful has been provided in Figure 7 as a plot between the inverse ratios of the mean slip distance parameters $1/\sqrt{\Lambda_s}$ and $1/\Lambda_g$. This plot shows that the slope relating these quantities remains a constant over the studied range of temperature *and* strain rate (later shown in Figure 10) and manifests as a linear relationship. The values for the -73ºC curve is not shown, however, as expected from Figure 6 the ratio does not hold for this low temperature. Again, this provides further evidence that a thermally activated mechanism is likely made thermodynamically unavailable at this low temperature, and the mean slip distance corresponding to geometrical dislocations is dramatically decreased. The utility of Figure 7 is the predictive ability for determining one slip distance parameter, given its counterpart. The presented method can now provide a completely concrete method for determining hardening parameters, where the method to determine Λ_s is outlined in Appendix B and Λ_g can be determined following Figure 7.

It has been accepted for decades that the statistically-stored dislocation content is dependent on geometrically-necessary dislocation accumulation as well as temperature and strain-rate (Ashby, 1970). Thusly, the relationship between the two slip distance parameters can be expected. In addition to this, the model also predicts the experimentally observed behaviour of the dislocation cellular structure with temperature and strain. This is an important mechanism that can influence a number of material properties from crack propagation to creep reduction. It is known that; (i) larger cells form at higher deformation temperatures and smaller cells at higher strains, (ii) the cell walls are comprised of dislocation tangles, where the dislocation density in the cell walls has been reported to be up to five times the average dislocation density, and (iii) cells formed at higher temperatures are more distinct–with thinner, well defined cell walls–than cells formed at lower temperatures (Staker and Holt, 1972; Thompson, 1977).

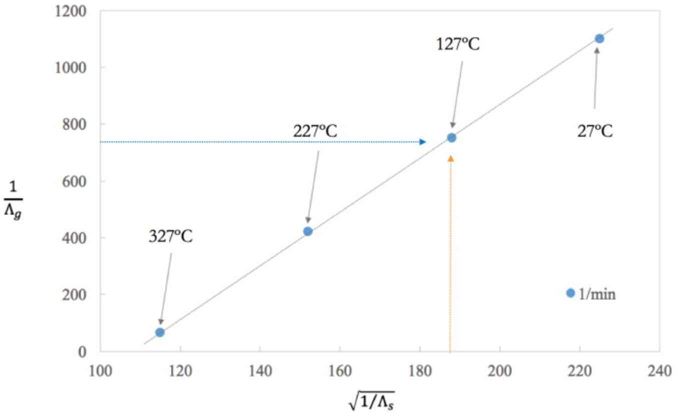

Fig. 7. A plot of the inverse of geometric slip distance parameter Λ_g versus the inverse root of statistical slip distance parameter Λ_s. The dotted line represents the constant predicted ratio between the two parameters over the studied temperature range.

3.4 Parametric Study

The model presented here is developed on the basis that the statistically stored-dislocations annihilate via dynamic recovery at the cell walls, and that the geometrically-necessary dislocations travel through the cell interior, accumulating at the cell walls, to accommodate shape change of the material. Therefore, the mean slip distance of the statistically-stored dislocations should be representative of an average dislocation density and always be less than the slip distance of geometrically-necessary dislocations, which is dependent on the cell size. During straining, simultaneous accumulation and recovery at the cell walls eventually reaches an equilibrium, whereby the cell walls remain at a relatively constant thickness. At low temperatures, this equilibrium may never be reached before failure, while at high temperatures this equilibrium state becomes evident.

Figure 8 represents this very well by plotting the stress from individual dislocation contributions. At $\Omega = 0$ the effects of recovery are removed and the curve over-predicts the strain hardening response upon sufficient dislocation accumulation at approximately 0.05 strain–a point related to the stage II-III transition. A recovery factor of $\Omega = 5.5$ provides the best fit to the experimental data at room temperature. The form of the model also affords the ability to distinguish the individual contributions of statistically-stored and geometrically-necessary dislocations, which–in nearly every modeling or experimental method–is either extremely arduous or impossible. This, however, is easily accomplished with the proposed model. At room temperature, the most hardening is due to statistically stored dislocations, which increase asymptotically at high strains. The geometric component, continues to grow more linearly at high strains indicating that the cell size of the substructure continues to increase with increasing strain.

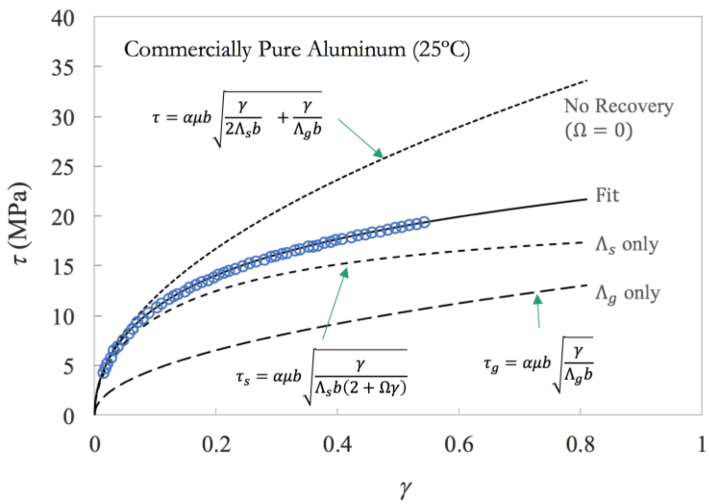

Fig. 8. Fitted – curve (solid line) and its match with the experimental 99.99% pure aluminum data at room temperature (Kocks 1976). The dashed lines show the individual contributions of the statistically-stored and geometrically-necessary dislocations according to the model.

3.5 Strain Rate Dependence

The explicit strain rate dependence is considered in the dynamic recovery formulation, as seen in equation (21). However, it must also be considered that, the mean slip distance parameters must also exude some rate dependence. The corollary between temperature and strain rate–whereby decreasing the deformation temperature will induce a similar behaviour as increasing the strain rate–also supports this. Since dislocation movement, recovery through vacancy climb, and annihilation are largely affected by thermodynamics, which is rate dependent itself due to diffusional processes, it is obvious that there must be rate dependence considered throughout. The uncertainty is predicting what the rate dependence should be for the mean slip distance parameters.

The simplest theory, is to assume a strain-rate dependence of the same distinction as with temperature. That is to assume that the inverse square-root of the statistically stored and inverse of geometric mean slip distance parameters behave in a linear fashion with strain-rate, as well as temperature. This is schematically shown in Figure 9, where the arrows denote the predicted change in slip-distance and recovery parameter with increasing strain rate. Due to diffusional considerations, it is also known that increasing strain-rate results in a decrease in mean slip distance of all dislocations. With this assumption, the results of increasing strain-rate should manifest as a linear translation upward of the inverse mean-slip parameters, creating a second linear set of points parallel to the low strain-rate data.

As a final measure of the predictability of the recovery model, stress-strain responses for pure aluminum at $\dot{\varepsilon} = 100/min$ strain rate are simulated and compared with experimental data. Initially, a single temperature data set is required to fit the new strain rate and then all subsequent temperatures can be predicted by the model. This is completed in the following, with room temperature data as the calibrating set.

A validation of the model can be completed for a new data set at a new strain rate. For this study, the available data from the work of Kocks (1976) on work hardening of pure aluminum provides data for the currently calibrated $\dot{\varepsilon} = 1/min$ strain rate in uniaxial tension, and the higher strain rate $\dot{\varepsilon} = 100/min$ in uniaxial tension. Therefore, the data is consistent and it can be assumed that there are no effects of varying texture or microstructure between test samples.

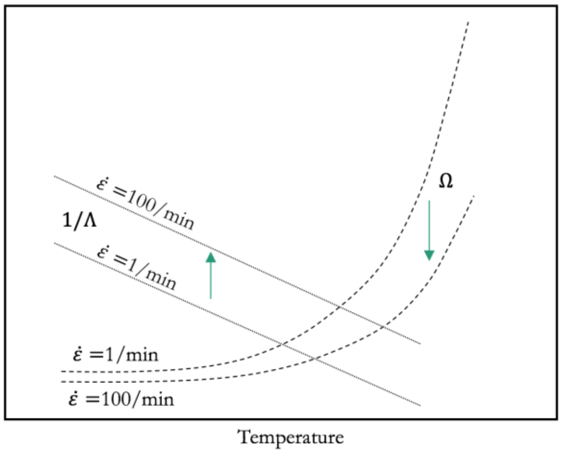
$\dot{\varepsilon}$ =100/min
1/Λ
$\dot{\varepsilon}$ =1/min
Ω
$\dot{\varepsilon}$ =1/min
$\dot{\varepsilon}$ =100/min
Temperature

Fig. 9. The vertical translation of slip distance parameters and recovery from $\dot{\varepsilon} = 1/min$ to $\dot{\varepsilon} = 100/min$ represents the strain-rate dependence of the mean slip distance parameters.

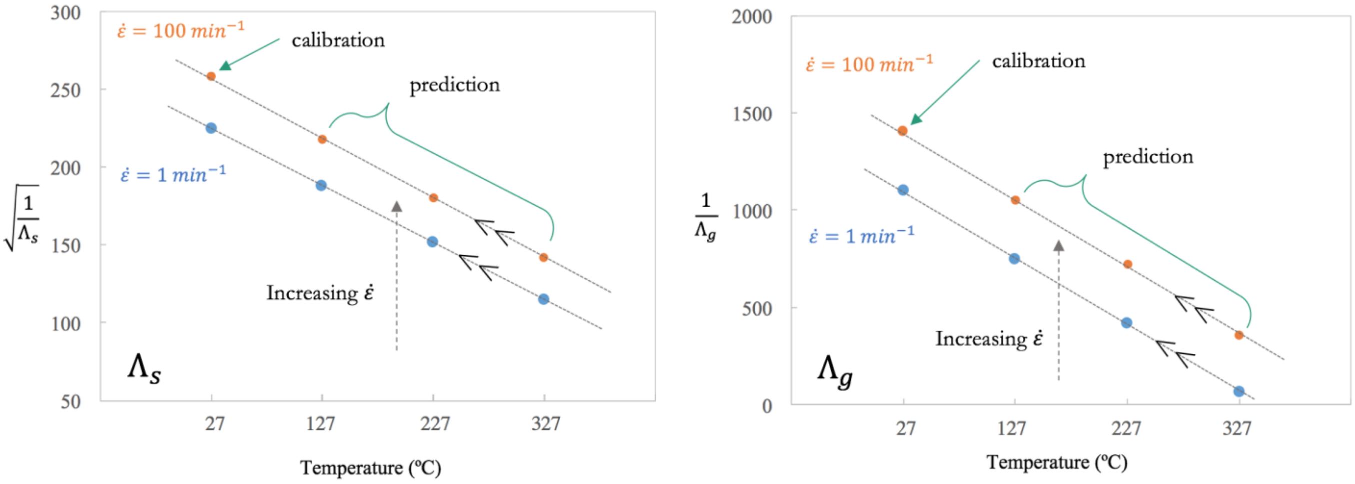

Fig. 10. The vertical translation of slip distance parameters from $\dot{\varepsilon} = 1/min$ (blue) to $\dot{\varepsilon} = 100/min$ (orange) represents the strain-rate dependence of the mean slip distance parameters. The room temperature slip parameters were first calibrated from the stress-strain curve fit, then the linear dependence of the parameters with temperature was used to predict the other three temperatures.

For calibration of the model at a new strain rate, only one test needs to be completed to determine the mean slip distance parameters. The simplest test is at room temperature, or 27ºC. The hardening parameters are determined firstly at this temperature using the procedure outlined in the previous sections. In Figure 10 the calibrated $\dot{\varepsilon} = 100/min$ slip distance parameters for Λ_s and Λ_g are labelled. The analysis predicts that the corresponding points for elevated temperatures fall on the line parallel to the $1/min$ data and passing through this newly calibrated $100\backslash min$ point. Two methods of verification can be employed: one where the elevated temperature parameters are measured and compared with expected results, the other is to predict these parameters from Figure 10 and compare the simulated and experimental stress-strain curves. The first method was chosen for convenience, and the results are presented for the mean slip distance parameters in Figure 10. The calibrated point at 27ºC is shown with a dotted line representing the expected values drawn parallel to the low strain-rate data. For both the geometrically-necessary and statistically-stored slip distance parameters, the results are in excellent agreement with the predicted values (dotted line).

The dynamic recovery factor, as with mean slip distance parameters, need only be calibrated one of two ways. The first through the theory outlined in section 2.1 and appropriately scaling previously measured low strain rate values to the higher strain rate. The second method requires two calibration points to determine the slope of the linear plot (Figure 11). The second method is simpler; however, it is ideal to have the ability to fit a new set of data with a single calibration. Given that the athermal recovery Ω_0 is constant with respect to temperature and strain rate, the recovery factor for other strain rates can be determined by solving equation (21). The low temperature recovery mechanisms embodied in as cross-slip is assumed to be strain rate independent, especially in the temperature range studied. As shown in Figure 5, the recovery at -73ºC is assumed to be purely due to the low temperature cross-slip mechanism. Therefore, the measured value at -73C is taken to be $\Omega_0 = 2.5$. The one third exponent is derived from the determination of average time for a vacancy to remobilize an immobile dislocation, however, the data collected suggests a weaker strain rate dependence. An optimized fit finds the rate sensitivity exponent to be equal to 1/5, which corresponds to the Nes and Marthinsen (2002) model for vacancy diffusion in courser grained pure FCC metals. Therefore, proper determination of the dynamic recovery factor can be given by

$$\Omega(\dot{\gamma}, T) = A_0 \left(\frac{D_0}{\dot{\gamma}}\right)^{1/5} \exp\left(-\frac{Q_m}{3RT}\right) \tag{24}$$

In Figure 11 the results for the calibrated points and expected decrease in recovery factor (dotted line) are presented. The relationship in equation (24) proves an accurate predictor of the recovery factor's rate sensitivity, as well as properly capturing the temperature dependence of moderate to high temperatures. It is interesting to note, possibly due to the low strength, that the increase in strain rate by a factor of 100 has nearly the same effect as decreasing the temperature by 100ºC. Similarly, the slip parameters Λ_s and Λ_g follow this trend. Physically, this suggests that the correspondence of temperature and strain rate are such that, for example, the deformation response is nearly identical between 127ºC at $\dot{\varepsilon} = 1/min$ and 500K at $\dot{\varepsilon} = 100/min$. This indeed does not consider the rate effects on fracture or damage and should not be mistaken as a suggestion that failure is also similar for these two conditions. This model is purely for deformation and does not consider any form of damage or other mechanisms leading to final failure or fracture.

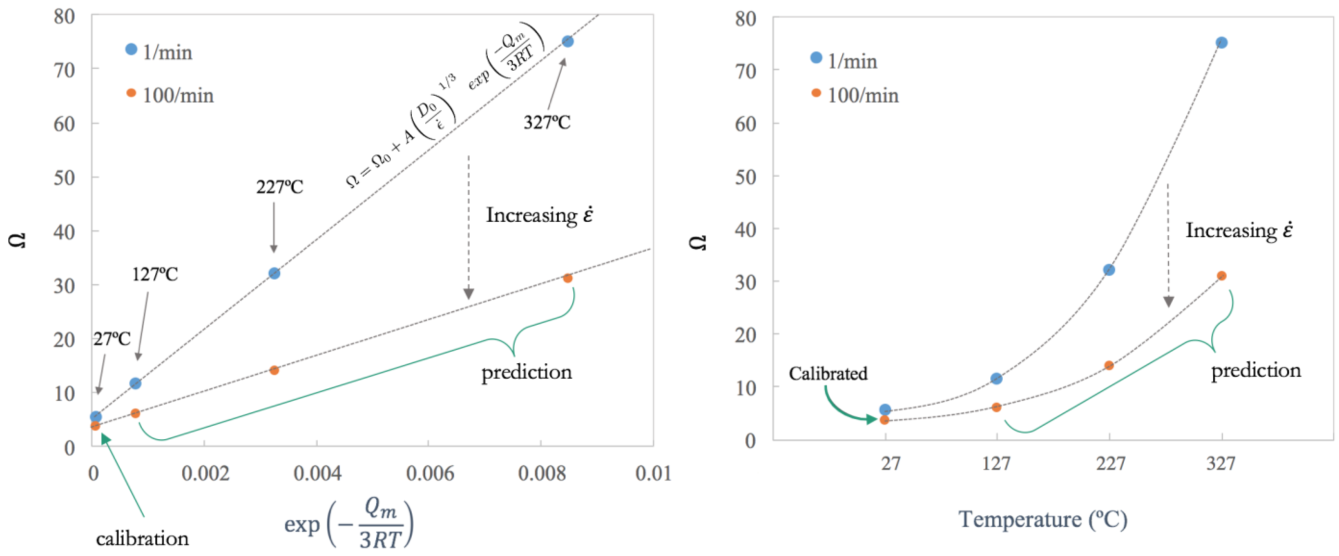

Fig. 11. The measured low strain rate (blue) and predicted high strain rate (orange) dynamic recovery factors for pure aluminum between 27ºC and 327ºC. The open point represents the calibrated recovery factor used to determine the predicted values (dotted line) at higher temperatures. Although -73ºC is not shown, the recovery factor at both strain rates corresponds to the same $\Omega_0 = 2.5$.

Lastly, the predicted shear stress-strain curves for the three elevated temperatures and the calibrated room temperature are presented in Figure 12. The predictions are very good and reflect the capability of the given model. The basis of dislocation and recovery theories that are used to develop the model are fundamental to achieving this. The model also presents the significance of both dislocation types–statistical and geometric–on determining the stress-strain response. In Figure 12, the experimental data provided for 227ºC and 327ºC was only available to approximately 10% engineering strain, however, the simulation results nonetheless have been extrapolated beyond the experimental data to showcase the high strain hardening predictions.

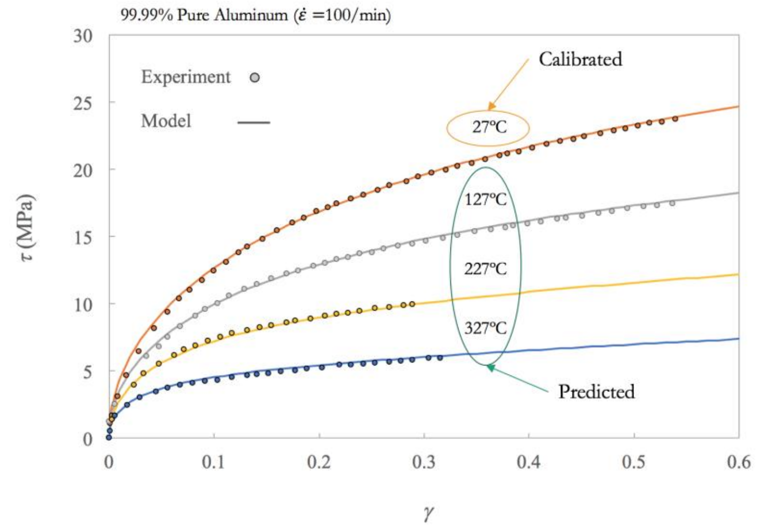

Fig. 12. Predicted shear stress-strain curves for the four high strain rate $\dot{\varepsilon} = 100/min$ and high temperature conditions corresponding to the material parameters shown in Figures 10 and 11. The 27ºC curve was calibrated to determine the high strain rate properties for the higher three temperatures. Experimental curves for 227ºC and 327ºC were only available to the strain value shown.

4. Implementation to Crystal Plasticity Theory

The well-known framework presented by Peirce, Asaro, and Needleman (1983) and reformulated by Cyr et al. (2015) to include thermal effects is employed in this research. The crystal plasticity framework can be condensed to a relationship used to update the shear rate on each slip system, denoted by $\dot{\gamma}^{\alpha}$, based on the currently resolved shear stress τ^{α} on the slip system α. Details of the single crystal constitutive model employed can be found in Inal et al. (2002) and Cyr et al. (2015). For completeness, a brief summary is presented in the following.

The total deformation is assumed to exist in three parts; (i) elastic part due to lattice distortion (including rigid rotation), (ii) thermal part due to expansion/contraction of the lattice, and (iii) plastic part as a result of dislocation motion and crystallographic slip. The numerical model incorporates 12 distinct slip systems for face-centered cubic (FCC) materials as principal deformation mechanisms. The elastic constitutive equation is written as:

$$\sigma_{ij}^{\nabla} = \mathbf{L}_{ijkl} D_{kl} - \dot{\sigma}_{ij}^{0} - \sigma_{ij} D_{kk} \qquad (25)$$

where σ_{ij}^{∇} is the Jaumann rate of Cauchy stress, $\mathbf{L}_{ijkl}$ is the elastic modulus tensor, D_{kl} is the strain rate tensor, and $\dot{\sigma}_{ij}^{0}$ is the viscoplastic-type stress rate, which depends on the slip rates.

4.1 Kinetics of Slip

The rate-dependent equation for single-slip shear rates is governed by the power law expression defined as,

$$\dot{\gamma}^{\alpha} = \dot{\gamma}_0 \operatorname{sgn}(\tau^{\alpha}) \left|\frac{\tau^{\alpha}}{\tau_y^{\alpha}}\right|^{1/m} \tag{26}$$

where $\dot{\gamma}_0$ is the reference shear rate assumed constant for all slip systems, τ^{α} is the resolved shear stress on slip system α, and τ_y^{α} is the temperature dependent slip system strength. The term $\operatorname{sgn}(\tau^{\alpha})$ denotes the sign of the resolved shear stress. Exponent $1/m$ is not to reflect physical behaviour of a rate sensitivity, but to conveniently ensure uniqueness of slip activity, which is spread over all available slip systems.

The rate of strain hardening of the crystal evolves by,

$$\dot{\tau}_y^{\alpha} = \sum_{\beta} h_{\alpha\beta} |\dot{\gamma}^{\alpha}| \tag{27}$$

where $\dot{\tau}_y^{\alpha}$ is the single slip hardening rate. The hardening moduli tensor $h_{\alpha\beta}$ depends on deformation history and accumulated slip and is written as,

$$h_{\alpha\beta} = q_{\alpha\beta} h_{\beta} \qquad (\mathit{no\ sum\ on}\ \beta) \tag{28}$$

Here $h_{\beta} = h_{\beta}(T)$ is a temperature dependent single slip hardening rate, and $q_{\alpha\beta}$ is the matrix describing the latent hardening behaviour. Asaro and Needleman (1985) considered the current hardness to evolve with total accumulated shear γ_{α} in the crystal such that,

$$\gamma_{\alpha} = \int_0^t \sum_{\alpha} |\dot{\gamma}^{\alpha}| dt \tag{29}$$

4.2 Strain Hardening

The hardening rate is derived from the flow rule equations developed in Part I and modified to include strengthening effects from solute Mg written as,

$$\tau = \alpha \mu b \sqrt{\rho_s + \rho_g + \rho_{Mg}} \tag{30}$$

The statistically-stored and geometrically-necessary dislocation densities ρ_s and ρ_g are determined from their respective slip distance parameters Λ_s and Λ_g such that,

$$\rho_s = \frac{\gamma_a}{\Lambda_s b (2 + \Omega \gamma_a)} \tag{31}$$

$$\rho_g = \frac{4\gamma_a}{\Lambda_g b} \tag{32}$$

The term ρ_{Mg} denotes the increase in stored dislocation content and material strength due to the addition of magnesium solute atoms as obstacles. In a similar manner that ρ_s and ρ_g have been related to the associated slip distance of dislocations, it is assumed that ρ_{Mg} will also exude a proportionality with the slip distance of dislocations impeded by solute atoms. The assumption is also made that this new slip distance parameter Λ_{Mg}, which is proportional to ρ_{Mg}^{-1}, does not evolve with strain and is directly related to initial microstructure. Therefore, increasing the concentration of solute Mg in the material will decrease the slip parameter; however, thermo-mechanical processing that alters the dispersion of solute atoms from the initial microstructure is assumed to not affect the effective slip-distance parameter.

Finally, equation (6) can be re-written in terms of mean slip parameters as

$$\tau = \alpha\mu b\sqrt{\frac{\gamma_a}{\Lambda_s b(2+\Omega\gamma_a)} + \frac{4\gamma_a}{\Lambda_g b} + \frac{1}{\Lambda_{Mg} b}} \tag{33}$$

where

$$\rho_{Mg} = \left(\Lambda_{Mg} b\right)^{-1}. \tag{34}$$

Hardening can then be easily determined by the work hardening of the above flow rule as in

$$h_\beta = \frac{d\tau}{d\gamma_a} = \alpha\mu b\frac{1}{2\sqrt{\rho}}\frac{d\rho}{d\gamma_a} \tag{35}$$

where ρ is the total dislocation density $\left(\rho = \rho_s + \rho_g + \rho_{Mg}\right)$. The new work hardening term $d\tau/d\gamma_a$ is dependent on experimentally determined parameters relating to the evolving microstructure and temperature written as

$$\frac{d\rho}{d\gamma_a} = \frac{2}{\Lambda_s b(2+\Omega\gamma_a)^2} + \frac{4}{\gamma_a b} \tag{35}$$

4.3 Critical Resolved Shear Stress (CRSS)

The crystal plasticity formulation requires an initial CRSS representing the undeformed yield strength of individual slip systems, denoted τ_{y0}. The developed model presented in this paper was used previously in Part I to show that $\tau_{y0} \approx 0$ for pure aluminum. For aluminum alloys, the initial CRSS is highly influenced by the alloying content and grain structure. In the presented model, the implied CRSS upon initial straining can be determined by evaluating the flow rule in equation (33) at zero accumulated strain (γ_a) such that,

$$\tau_{y0} = \alpha\mu\sqrt{\frac{b}{\Lambda_{Mg}}} \tag{36}$$

Following this, the term Λ_{Mg} can now be determined directly from the yield of the experimental stress strain curve.

4.4 Solute Drag

Aluminum alloys of the 5xxx (Al-Mg) series are considered non-heat-treatable alloys, and therefore great candidates for warm forming for structural components. Deformed Al-Mg alloys are characterized by relatively even distribution of dislocations due to an effect known as solute drag. This prevents re-arrangement of dislocations into lower energy structures and increases the work hardening rate. In fact, in Al-Mg systems, the solute drag effect is greater on work hardening than solution strengthening (Park & Niewczas, 2008). Lower temperature produces a similar effect, and it has been observed that this temperature effect is more sensitive in low solute alloys rather than highly alloyed systems. This reflects competing mechanisms of dynamic recovery and solute drag.

In essence, the solute drag effect is the disruption or impedance of dislocation motion due to solute Mg atoms. Upon sufficient energy and dislocation pile-up near solute particles, the dislocations suddenly pass the solute obstacle. The diffusion of Mg in the Al matrix facilitates this sudden passage of dislocations. Optimal conditions for solute drag to take effect are at sufficiently low temperatures while Mg still remains in solution and intermediate strain rates (on the order of 10^{-4} to 10^{-2} s^{-1}). At high strain rates, dislocation motion carries enough energy to sweep past the Mg obstacles, while at sufficiently low strain rates or high temperatures diffusion of Mg prevents drag. In the following, the experimental data falls inside this intermediate strain rate range, and the effect of the Mg solute drag can be observed as "jerky flow" at room temperature. Uniaxial tension data above 25ºC, up to 121ºC (not shown in Figure 14) fall nearly coincident. Although the increasing recovery should be lowering the stress-strain curves, the competing solute drag works to stabilize the work hardening over a significant temperature range. Above this temperature (148ºC) at the given strain rate, the "jerky flow" behaviour ceases and the material flows virtually uninhibited by Mg solute atoms.

4.4.1 Numerical Implementation

To capture the effects of solute drag in crystal plasticity, the kinetics of the slip formulation must be modified. Since this mechanism affects the actual motion of dislocations, and not necessarily the dislocation production or recovery, the solute drag effect is connected directly to the shear slip rate equation (26). In the current formulation, each slip system allows slip as determined by the ratio of the resolved shear stress to the slip system strength. From the discussion above, some amount of slip must be stopped until a threshold is reached. Over this threshold, slip is allowed to occur at an accelerated rate, resulting in a "jerky flow" behaviour. Thus, equation (26) can be rewritten to show

$$if\,\frac{\tau^{\alpha}}{\tau_y} < f_c \qquad \dot{\gamma}^{\alpha} = \dot{\gamma}_0 \tag{37a}$$

$$if\,\frac{\tau^{\alpha}}{\tau_y} \geq f_c \qquad \dot{\gamma}^{\alpha} = \dot{\gamma}_1 \mathbf{sgn}(\tau^{\alpha}) \left|\frac{\tau^{\alpha}}{\tau_y^{\alpha}}\right|^{1/m} \tag{37b}$$

where $f_c < 1$ is the critical ratio for slip on a given system α. For this work, it will be assumed that all slip systems accept the same critical parameter. The term $\dot{\gamma}_1$ represents the reference shear rate once slip has been allowed to occur. In order to lead to the "jerky flow" behaviour, this $\dot{\gamma}_1$ parameter must be sufficiently large, and decay to $\dot{\gamma}_0$ as temperature is increased. Similarly, f_c will decay to a value sufficiently small as temperature is increased such that drag is negligible.

In Figure 13, the effect of solute drag kinetics on the presented crystal plasticity simulation at room temperature is presented. For the entire polycrystal simulation, consisting of 1000 crystal orientations, the "jerky flow" behaviour cannot be observed due to the Taylor averaging of individual crystal; however, this effect can be seen when the number of crystals is reduced. The jerky flow curve was generated using a sample of 10 nearly cube orientations to demonstrate the individual crystal effect. The amplitude of the stress oscillations and the frequency are determined by the magnitude of $\dot{\gamma}_1$ and f_c, which are related to experimental conditions of temperature and strain rate as well as the solute content. The correlation between these parameters and experimental conditions are beyond the scope of this work; however, the results were obtained in the range of $(0.7 < f_c < 0.9)$. The main focus of this study is using a fully consistent model to predict temperature dependency of microstructural parameters leading to material hardening. In addition, the solute drag effect is not apparent in warm forming conditions, so for this study is only considered in the room temperature simulations and equation (26) is employed for all elevated temperature simulations.

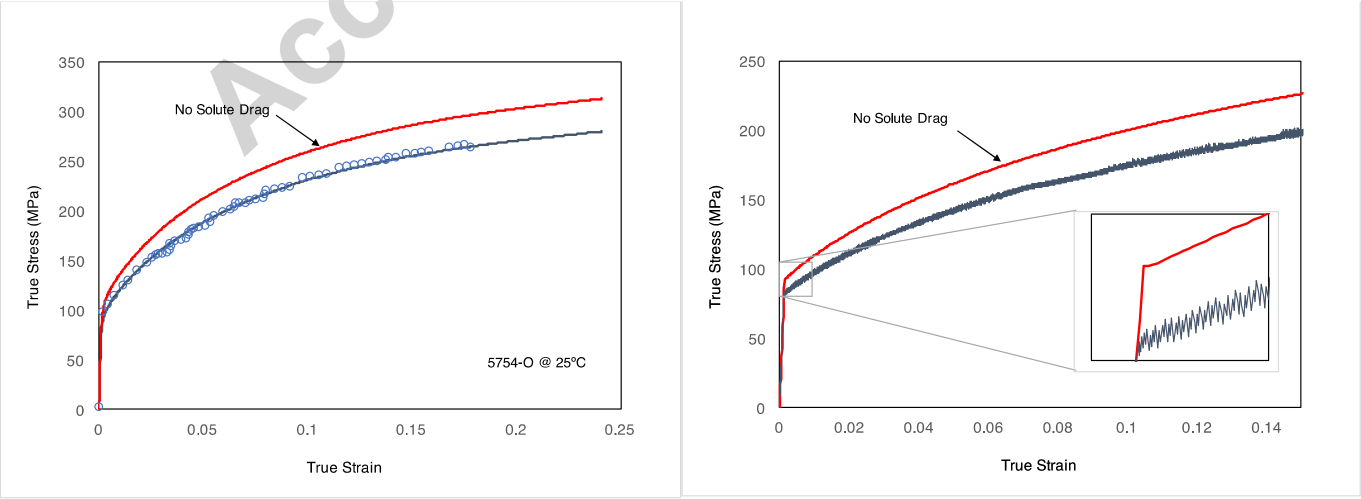

Fig. 13. (left) Stress-strain curves with and without the solute drag effect for the simulated polycrystal and (right) cube single crystal at room temperature. For simulating solute drag $f_c = 0.85$ and $\dot{\gamma}_1/\dot{\gamma}_0 = 10^6$ was employed.

4.5 Chemical Composition of AA5754-O and AA5182-O

A Taylor polycrystal averaging scheme is employed in a crystal plasticity framework (Cyr et al., 2015) to simulate uniaxial tension for aluminum sheets AA5754-O and AA5182-O. The reported chemical composition of these two simulated alloys is presented below in Table 2. This crystal plasticity approach provides a fast method to account for grain interactions and morphologies providing more realistic predictions of strain partitioning due to the microstructure.

Table 2 Chemical composition of aluminum alloys (wt%).

	Mg	Mn	Fe	Si	Cu	Ni	Ti	Zn	Al
AA5182-O	4.3	0.34	0.21	0.03	<0.01	<0.01	<0.01	<0.01	Balance
AA5754-O	3.0	0.24	0.26	0.03	0.02	<0.01	<0.01	<0.01	Balance

4.6 Stress-Strain Curves and Initial Texture

The uniaxial tension stress–strain data used for the determination of the material parameters for the presented models is obtained from work published by Abedrabbo et al. (2007). The digitized true stress-true strain data is presented in Figure 14 for AA5754-O and AA5182-O over a range from temperatures between 25ºC and 260ºC at constant strain rate $\dot{\varepsilon} = 0.0083\ s^{-1}$ ($\dot{\varepsilon} = 0.5/\mathrm{min}$). This dataset was chosen since the material used for measurements is very similar to the material used to generate the simulated texture. The AA5754-O dataset is used to study temperature dependence of the model parameters, followed by testing the predictive capability of the new formulation on the AA5182-O data.

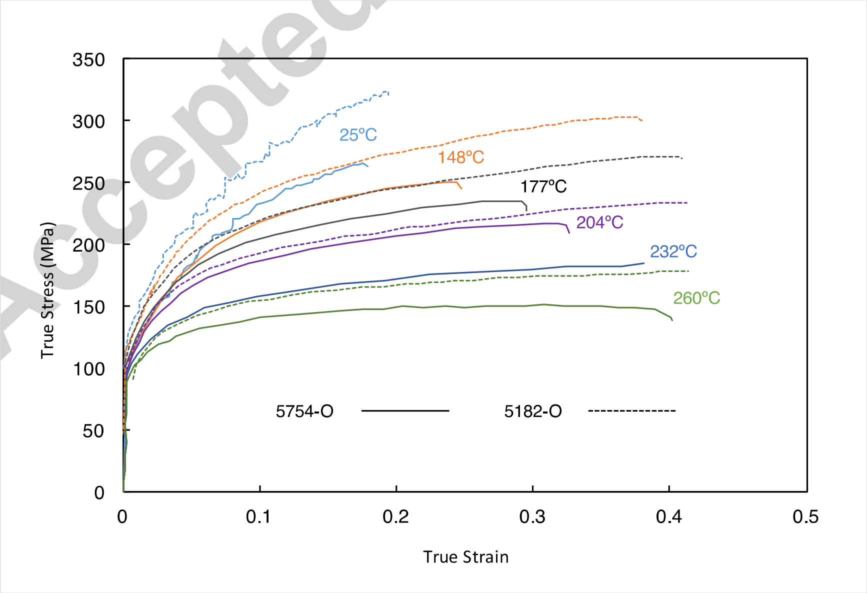

Fig. 14. Experimental true stress-true strain curve (reproduced from original data published in Abedrabbo et al., 2007).

The initial texture used for simulation of both materials is shown in Figures 15 and 16 in the form of a {111} recalculated pole Figure (PF) and orientation distribution function (ODF) respectively. The pole Figure shows that the sheet has a reasonably weak texture with the peak intensity at approximately 1.8 times random. Both the pole Figure and ODF show presence of mostly Cube with some Brass components. In the ODFs Cube intensity is the highest at 3.1 times random while intensity of Brass component is at 1.2 times random.

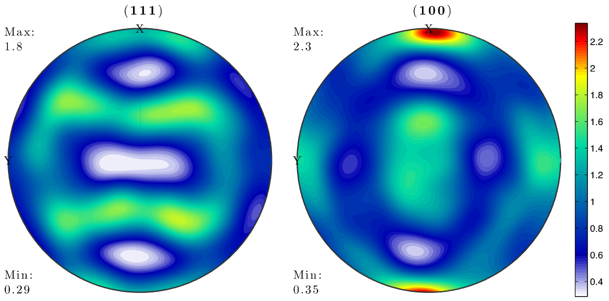

Fig. 15. (111) and (100) recalculated pole Figures of rolled sheet AA5754-O used as input. Axes directions X and Y correspond to RD and TD directions, respectively.

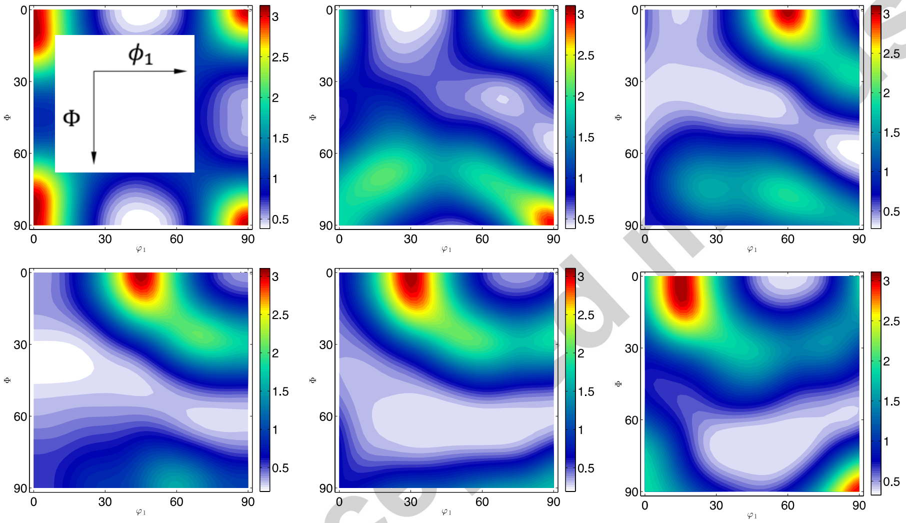

Fig. 16. ODF sectioning with 15º sections of ϕ_2 from 0º to 75º of the input AA5754-O sheet texture. The ODF shows rotated cube and some copper and brass components, typical of rolled and annealed sheet.

5. Results

The simulated uniaxial tension curves at the six different temperatures with the experimental curves are presented in Figure 17 for AA5754. It is important that the model capture the hardening behaviour along the entire stress-strain curve to be able to correctly characterize the material parameters. The effective yield strength is a contribution of the initial texture, as well as the parameter Λ_{Mg}. The initial hardening is most strongly influenced by the mean-slip distance of statistically-stored dislocations, while the high-strain hardening is governed by geometrically-necessary slip and recovery of the statistically-stored dislocations. The material parameters used in these simulations are presented in Table 3. These parameters were obtained by the methods described in the previous sections.

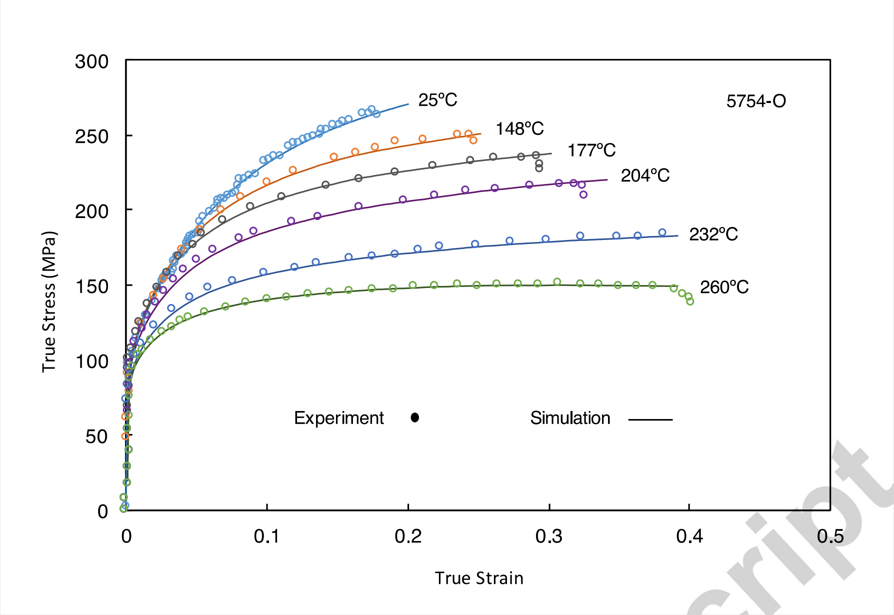

Fig. 17. Simulated stress-strain curves at 25ºC, 148ºC, 177ºC, 204ºC, 232ºC, and 260ºC and experimental data plotted as points.

Table 3. Hardening parameters from AA5754-O simulated uniaxial tension tests. Slip distance parameters are in units of microns and were calculated from their inverse.

Temp. (*°C*)	Λ_s (*μm*)	Λ_g (*μm*)	Λ_{Mg} (*μm*)	Ω
25	0.756	50.0	26.3	3.0
148	0.756	50.0	26.3	6.5
177	0.756	50.0	26.3	8.0
204	0.907	50.0	26.3	10
232	1.108	76.92	30.3	13
260	1.181	117.6	30.3	17

5.1 Temperature Dependency of Material Parameters

Figure 18 shows a graphical representation of the slip parameters presented in Table 3 for AA5754 and their temperature dependency. The data shows that decreases in hardening at temperatures near room temperature are completely governed by recovery. This contradicts findings for pure aluminum where slip-distance parameters show a temperature dependency in the entire temperature range studied. This suggests a strong influence of the material's alloying in the stabilization of microstructural parameters over low to intermediate temperatures. At sufficiently high temperatures; however, the slip-distance parameters begin to reclaim their temperature dependency. At the highest simulated temperatures, the parameter Λ_{Mg} also loses stability and begins to increase. It is believed that this is due to diffusion of Mg to high energy regions, such as grain boundaries, effectively reducing the strengthening due to dispersed Mg (Niewczas *et al.*, 2015).

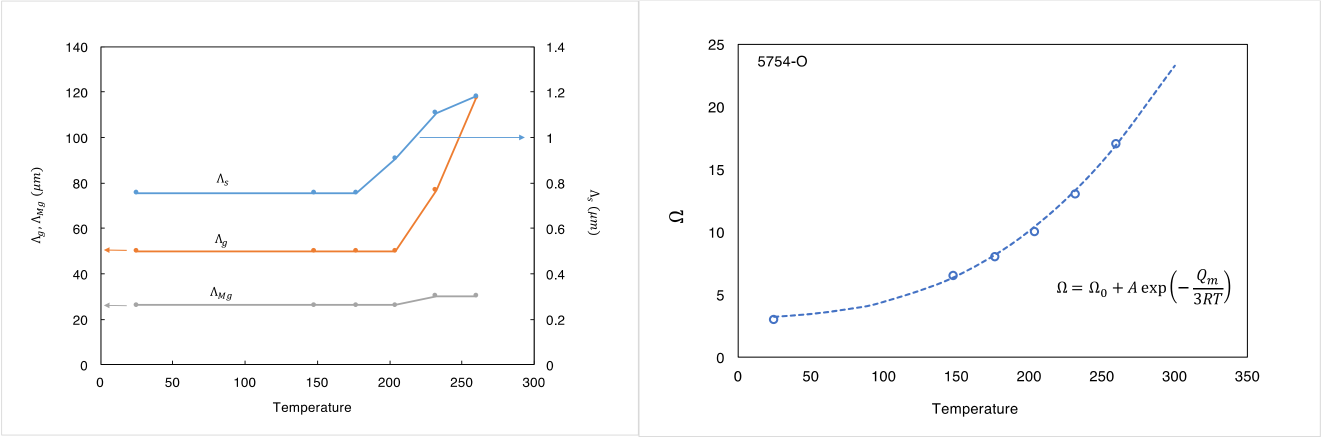

Fig. 18. (left) Temperature dependency of mean slip distance parameters for simulated AA5754-O. (right) Temperature dependency of dynamic recovery factor for simulated AA5754-O with exponential according to equation (21). Fitting constants were determined to be $\Omega_0 = 3.0$ and $A = 2.9 \times 10^3$.

5.2 Mechanical Response of AA5182-O

Due to the similarities of the two materials, it is assumed that both will behave similarly in terms of their temperature dependencies. The AA5182 alloy has increased yield strength due to higher alloying, which can be captured by the Λ_{Mg}. AA5182 also experiences somewhat higher hardening than AA5754 suggesting a minor difference in Λ_s and Λ_g between the two alloys. It is also assumed that the experimental preparation for both alloys was conducted in a similar fashion, such that their differences in texture and microstructure (grain size and shape, etc.) are negligible. Therefore, the same simulated texture, presented in Figures 15 and 16 will be used for AA5182. Lastly, the recovery parameter should not significantly vary due to the composition similarities. However, the increase in Mg content in AA5182 may increase recovery by facilitating remobilization of immobile dislocations. Athermal recovery Ω_0 and the constant A should therefore increase.

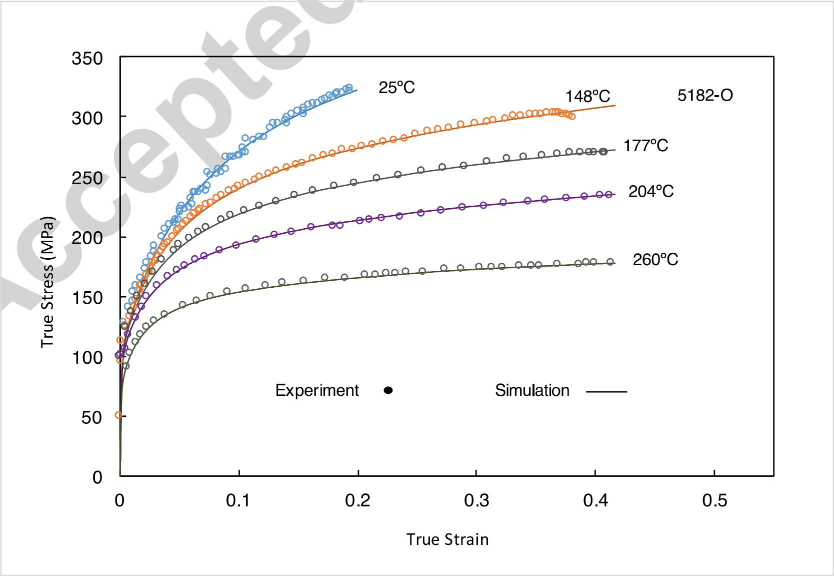

Fig. 19. Simulated stress-strain curves at 25ºC, 148ºC, 177ºC, 204ºC, and 260ºC and experimental data plotted as points.

Presented in Figure 19 are the simulated stress-strain curves for AA5182 as well as experimental points extracted from Abedrabbo et al. (2007). Material hardening constants were initially calibrated to the intermediate 148ºC data and 204ºC data. From this, and the predictions gathered from the AA5754 simulations, the other hardening parameters were extrapolated. The simulated hardening parameters are presented in Table 4. The 5182 data-set did not have stress-strain data for 232ºC.

Table 4 Hardening parameters from 5182-O simulated uniaxial tension tests. Slip distance parameters are in units of microns and were calculated from their inverse.

Temp. (ºC)	Λ_s (μm)	Λ_g (μm)	Λ_{Mg} (μm)	Ω
25	0.64	15	22	4.0
148	0.64	24	22	8.0
177	0.64	31	22	10.5
204	0.69	42	22	13.5
260	0.69	77	37	22

6. Discussions

It should be mentioned that all discussions presented below are based on the unique set of parameters obtained from the procedure explained Appendix B. The analysis shows that the developed formulation is able to capture the entire stress-strain behaviour very well at all temperatures investigated. Here, the determined material parameters will be used to discuss the effects of Magnesium additions and temperature on the two studies alloys.

6.1 Influence of Mg on Temperature Dependency

In Figure 20 the temperature dependency is plotted for the three slip-distance parameters for AA5182 with AA5754 for comparison. The behaviours of Λ_s and Λ_{Mg} show exact similarity to the results obtained for AA5754. The increased Mg content in AA5182 contributes to decreasing mean free path for all dislocations types and therefore strengthens the material. With the exception of Λ_g for AA5182, the mean slip distance is very stable over temperatures up to 200ºC, and all thermal softening is developed by dynamic recovery of dislocations. Above 200ºC, the model suggests that the microstructure begins to lose its order, allowing for greatly increased dislocation movement. The mean slip distance Λ_{Mg} shows that this is most likely due to Mg diffusion (Chen *et al*. 2016). While at low temperatures, the Mg can facilitate the subgrain structures, such as cellular formation and development of sub-grain boundaries that effectively maintain the dependency of Λ_s and Λ_g on the distribution of Mg atoms, and less on temperature. At sufficiently high temperatures, where Mg can diffuse easily to, for example, grain boundaries, these stabilizing effects of Mg are lost and slip of geometrically-necessary and statistically-stored dislocations begin to grow rapidly as the subgrain structures are absolved. There is one parameter, however, that argues this idea. For the 4.3 wt% Mg AA5182, Λ_g is never stable and exudes a temperature dependency over the entire temperature range studied. As temperature decreases, Λ_g continues to decrease as well, contributing to increased work hardening of the AA5182 alloy. This is the most significant difference between these two materials. It is known that higher Mg alloys will increase work hardening (Niewczas *et al*. 2015), however, this model predicts the underlying cause to be the increasing strengthening due to geometrically-necessary dislocations. In AA5182, the increased Mg content may diffuse to form less random distributions or clustering at lower temperatures weakening the subgrain structures and allowing Λ_g to grow more easily. It is likely this greatly increased work hardening from geometrically-necessary dislocations in AA5182 that give way to its high ductility at intermediate temperatures, compared to AA5754.

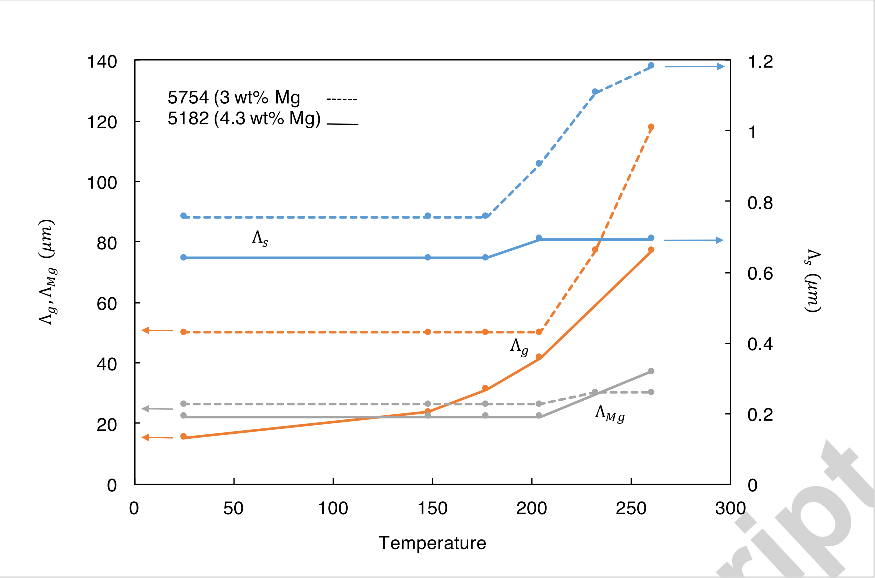

Fig. 20. Temperature dependency of dynamic mean slip-distance parameters for simulated AA5182-O and AA5754-O for comparison.

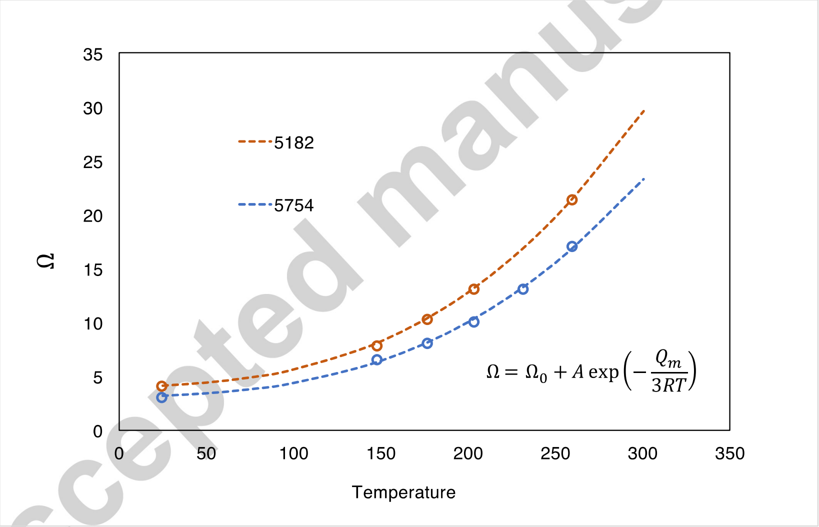

Fig. 21. Temperature (ºC) dependency of dynamic recovery factor for simulated AA5182-O and AA5754-O for comparison with equation (21). Fitting constants for AA5182 were determined to be $\Omega_0 = 3.5$ and $A = 3.9 \times 10^3$.

Dynamic recovery presented in Figure 21 shows little variation between the two alloys. Increased Mg content increases the recovery for AA5182 over the entire temperature range as predicted in the previous section. Of the possibly explanations for this behaviour, the most likely is that Mg atoms contribute to the remobilization of immobile dislocations in a similar manner to vacancies. Elastic strains due to lattice mismatch near Mg solute may also attract vacancies, increasing the Mg diffusion. The effect of Mg, however, must be minimal due to the similarity of recovery factors between the studied alloys and pure aluminum.

Physically motivated hardening models derived from dislocation theories and micromechanics have been developed previously (Nes, 1998; Nes and Marthinsen, 2002; Rotors, Raabe and Gottstein, 2000) beginning with same relation for balance between production, storage, and annihilation of dislocations; however, the derivation of parameters and the way they evolve with the flow stress is approached differently. Mainly, they considered both dislocation density in cell interiors and cell walls explicitly requiring a significantly greater number of material constants/parameters. They also suggest a definitive transition from stage II to III type hardening, which is difficult to determine in polycrystalline metals. In addition to these differences, this study also presents a simple formulation to implement the proposed model into a crystal plasticity framework to account for slip-rate dependent mechanisms such as solute drag in AA5754, which has not been done in the above articles. The proposed model is also much simpler to calibrate and implement than previously developed models while still considering the micromechanical physical phenomenon that causes the macroscopic material behaviour. It only requires the same calibration stress-strain data as a simple power-law hardening model, with few constants, but can provide as much insight and knowledge of the material structure and micromechanical behaviour as the more complex and difficult to calibrate Nes and Marthinsen, and Rotors, Raabe, and Gottstein models.

Conclusions

In this study, a physical and mechanistic theory is derived based on the thermodynamic and mechanical balance between dislocation storage, accumulation, annihilation and recovery for a polycrystalline material. The theory is then developed into a new three-parameter constitutive model and hardening law for simulating flow stress, and pure aluminum stress-strain data is used to calibrate the model and investigate temperature dependency of model parameters. The model is then implemented into a temperature dependent crystal plasticity framework to study two Al-Mg alloys. The model is modified to include solution strengthening effects due to Mg additions and written in a rate form hardening law for simulating flow stress. The temperature dependence of hardening parameters embedded in the theory have been calibrated and presented with experimental data of AA5754-O and AA5182-O from 25ºC up to 260ºC. The temperature dependence of the hardening behaviour can be summarized by four important material parameters: mean slip distance of statistically-stored Λ_s, geometrically-necessary Λ_g dislocations and the dynamic recovery factor Ω. The fourth is the alloy specific parameter Λ_{Mg} parameter representing mean slip of dislocations impeded by solute Mg. The following was concluded from the study:

- The material hardening parameters can be measured directly from the experimental stress-strain curves with the exception of the dynamic recovery factor which must be calibrated.
- The model can predict very well the stress-strain response of a large range of temperatures and at least of intermediate strain rates of $\dot{\varepsilon} = 1/min$ and $\dot{\varepsilon} = 100/min$.
- Dynamic recovery can be predicted from an Arrhenius-type relationship for the remobilization of immobile dislocation by vacancy climb and is temperature and strain-rate dependent.
- The contributions of the material hardening parameters as well as contributions of statistically stored and geometrically necessary dislocation densities via their Λ-parameters can be extracted easily using the model.
- Analysis of the temperature dependence of mean slip distance parameters show graphically an inverse square root proportionality of Λ_s and an inverse proportionality of Λ_g that is consistent at different intermediate strain rates. In addition, the proportionality of these two slip parameters is also constant for all studied warm temperatures and strain rates allowing for the prediction of one parameter given the other.
- There is a unique set of material hardening parameters that can be measured directly from the experimental stress-strain curves by the procedure (outlined in Appendix B) with the parameter Λ_{Mg} determined from $\tau_{y0} = \alpha\mu\sqrt{b/\Lambda_{Mg}}$.
- The model is able to provide excellent fits to experimental data and good predictions of material hardening behaviour and temperature dependency.

- Dynamic recovery can be predicted from an Arrhenius-type relationship for the remobilization of immobile dislocation by vacancy climb with minimal calibration.
- The temperature dependency microstructural mechanisms governed by mean slip distance of dislocations is highly complex and difficult to determine a single temperature dependency in an alloyed polycrystalline system – unlike with pure aluminum. However, it can be concluded that Mg additions are able to stabilize microstructure at intermediate temperatures (below 175ºC-200ºC) leaving dynamic recovery as the sole mechanisms driving temperature dependence of stress-strain response.
- Graphical analysis of the temperature dependence of mean slip distance parameters show that above approximately 175ºC to 200ºC there is a change in microstructure stability that allows for a sudden increase in dislocation mean free path for all types of dislocations. This is attributed to diffusion of solute Mg atoms facilitating the weakening of substructures, such as cell walls, and becoming significantly weaker obstacles themselves. The may also begin to diffuse to grain boundaries allowing for increased mean slip distance within grains.
- To capture the correct hardening response at room temperature, the effect of solute Mg on dynamic strain aging/solute drag must be accounted for. Without this effect, the model predicts an unrealistic decrease in hardening with decreasing temperature from 148ºC to 25ºC.

Acknowledgements

This work was supported by the Natural Sciences and Engineering Research Council of Canada (NSERC) and General Motors of Canada. The authors would also like to thank Dr. Merek Niewczas for his collaborative discussions and expertise.

Appendix A: Recovery Factor

A relationship is needed for the number of vacancies that will reach the cell walls after some given time t, which will be denoted $\mathcal{N}$. This must be proportional to the density of vacancies n_0 and the average distance δ a vacancy has migrated after some time. Considering that a vacancy can approach the cell walls from either direction, the relationship can be written as

$$\mathcal{N} = 2n_0\delta = 2n_0\sqrt{2Dt} \tag{A1}$$

According to the assumptions made previously, the remobilization of sessile dislocations in the cell walls is conducted via vacancy climb, therefore it is reasonable that recovery, or $\Omega(\dot{\gamma}, T)$, is proportional to the number of vacancies reaching the cell walls such that

$$\Omega(\dot{\gamma}, T) = \mathcal{K}n_0\sqrt{2Dt} \tag{A2}$$

with $\mathcal{K}$ representing a proportionality constant (including the factor of 2 from equation (19)).

Finally, we must determine an expression for the time dependence, t. If the average distance a vacancy travels in time t is given by equation (20), then an average time can be found for a dislocation to travel a distance δ. Therefore, we introduce the concept of average wait time, or the time between successive remobilizations of immobile dislocations. As recovery increases, it is expected that the mean wait time between these remobilizations will decrease. Letting $\bar{t}$ denote the average wait time, equation (21) can be rewritten as

$$\Omega(\dot{\gamma},T) = \mathcal{K}n_0\sqrt{2D\bar{t}} \tag{A3}$$

Now assume, by differentiation of equation (11) with respect to time, that the rate of dislocation remobilization is $d\rho/dt = -\Omega\rho\dot{\gamma}$. Assuming an initial dislocation content of the unstrained material as ρ_0, integration yields

$$\rho(t) = \rho_0 \exp(-\Omega\dot{\gamma}t) \tag{A4}$$

The average wait time of the immobile dislocations can now be determined by the following:

$$\bar{t} = \frac{\int_0^\infty t\rho(t)dt}{\int_0^\infty \rho(t)dt} = \frac{1}{\Omega\dot{\gamma}} \tag{A5}$$

If we only consider thermal component of the total recovery, then $\bar{t}$ can be written as

$$\bar{t} = \frac{1}{\Omega(\dot{\gamma},T)\dot{\gamma}} \tag{A6}$$

and can be inserted back into equation (21) yielding

$$\Omega(\dot{\gamma},T) = \mathcal{K}n_0\left(\frac{2D}{\Omega(\dot{\gamma},T)\dot{\gamma}}\right)^{1/2} \tag{A7}$$

Lastly, solving for $\Omega(\dot{\gamma},T)$ and replacing D with its Arrhenius relationship gives

$$\begin{aligned}\Omega(\dot{\gamma},T) &= \left(\mathcal{K}n_0(2D_0)^{\frac{1}{2}}\right)^{2/3} \exp\left(-\frac{\backslash Q_m}{3RT}\right)\dot{\gamma}^{-1/3} \\ &= A_0\left(\frac{D_0}{\dot{\gamma}}\right)^{1/3} \exp\left(-\frac{Q_m}{3RT}\right)\end{aligned} \tag{A8}$$

where A_0, which is proportional to $(\mathcal{K}n_0)^{2/3}$, is the only unknown parameter. The values of D_0, Q_m, and R are tabulated data, and temperature and strain rate are from experimental conditions.

Appendix B: Determination of Hardening Parameters

The benefit of this model is that the fitting procedure ensures the correct set of material parameters are chosen. There may be more than one set of parameters that provide an adequate fit to stress-strain data, however, this model guarantees the correct parameter set therefore ensuring these parameters represent the actual microstructural phenomenon and can be used to predict or infer understanding of the microstructural behaviour.

In the presented model, the material hardening depends on experimentally determined parameters relating to the evolving microstructure. Parameters λ_s, λ_g, $1/\phi$ and P/A are initially assumed to behave independent of temperature and are calculated from room temperature experimental data. Recovery represented by Ω is determined according to the high-strain hardening behaviour at multiple temperatures to validate the temperature dependent equation (28). The procedure proposed to obtain these values is described in this section.

Firstly, stress-strain data is fit by a polynomial function (up to 5th or 6th order), and the value of σ_0 is first assumed as the zero-strain intercept of the polynomial function, as shown in Figure B1. From this, the flow shear stress $\tau = (\sigma - \sigma_0)/M$ versus the shear strain $\gamma = M\varepsilon$, where M is the Taylor factor such that $M = 3$ for this analysis, can be plotted.

The flow stress is related to the retained dislocation density ρ by the strength of obstacle parameter α, and therefore can be determined experimentally from the $\log(\tau)$ *vs.* $\log(\rho)$ plot. However, the difficulty is measuring the retained dislocation density, whereby it is challenging to resolve dislocation density from other deformation debris (Saimoto, 2006). This leads to an under/over prediction of the dislocation content depending on the measuring method chosen

(Schafler, 2005). However, an obstacle strength for aluminum of approximately 0.35-0.45 has been widely published (Hirth and Lothe, 1967; Saimoto, 2006; Park and Niewczas, 2008) and a value of 0.4 is assumed for this study.

For the determination of mean slip distance, it must first be assumed that under ideal conditions, during yielding the statistically-stored dislocation mean slip distance is equal to the interobstacle spacing, which is equal to the inverse root of retained dislocation density, i.e. $\lambda_s = \ell = \rho^{-1/2}$, therefore, allowing the relation $\ell = \alpha\mu b/\tau$. From the experimental flow stress, the mean slip distance λ_s is then calculated by equation (3) and plotted. The slope of $d\tau/d\gamma$ is calculated as the instantaneous slope of the τ *vs.* γ polynomial. The value of $1/\phi$ is then optimized such that the curves of $\log(\lambda)$ and $\log(\ell)$ plotted against $\log(\tau)$ are equal for the lowest value of τ, as presented in Figure B1. For this analysis, the minimum value of λ_s is chosen as the characteristic mean slip distance. This has been hypothesized to correspond to the transitional point between stage II and stage III hardening (Saimoto and Van Houtte, 2011). The apparent transitional increase in mean slip distance is attributed to the formation of cellular structures and recovery mechanisms. In the cell interiors, a lack of retained dislocation content increases the mean free path that dislocations can propagate before encountering an obstacle. However, the fact that activation work rather than a specific flow stress governs thermal activation allows this averaging procedure between cell walls and interiors, thus the mean slip distance can be approximated as a constant λ_{min}. This minimum slip distance is associated with the statistically-stored dislocations given that, at low strains, the relative slip distances are such that $\lambda_s \ll \lambda_g$.

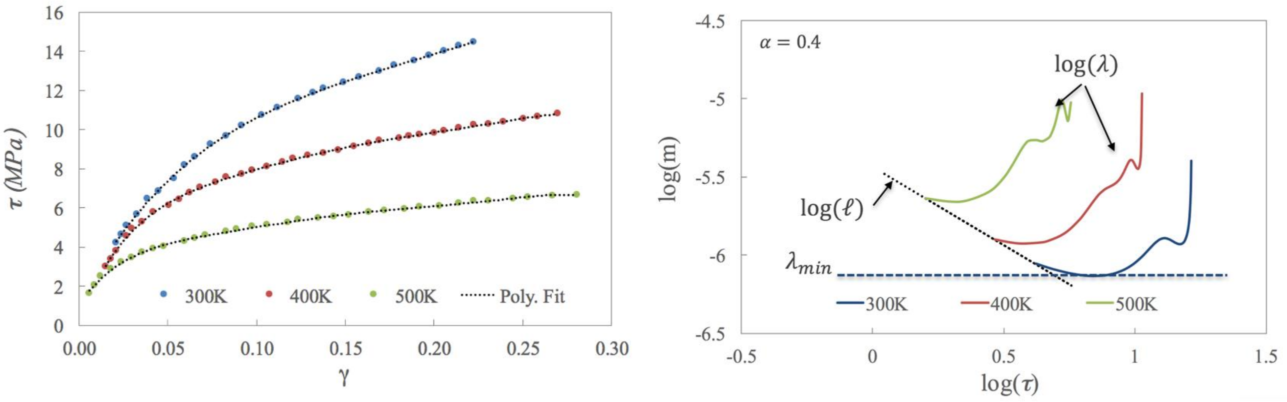

Fig. B1. (left) polynomial fit to experimental stress-strain data of pure aluminum and (right) $\log(\lambda)$ and $\log(\ell)$ jointly plotted *vs.* $\log(\tau)$ with ϕ^{-1} adjusted to match $\log(\lambda)$ and $\log(\ell)$ at low strains. The dotted tangent line depicts the minimum mean slip distance λ_{min}. The experimental stress-strain data is taken from Kocks (1976).

Finally, P/A is determined by examination of the constitutive relations. Upon yielding, equation (3) can be integrated to the following form

$$\tau = \left(\frac{\phi}{\lambda_s} b\mu^2\gamma\right)^{1/2} \tag{B1}$$

Equating this to the constitutive relation in equation (14) yields

$$\frac{\phi b\mu^2}{\lambda_s} = \frac{P}{A}\frac{(\alpha\mu b)^2}{\lambda_s b}\frac{1}{2+\Omega\gamma} \tag{B2}$$

and the small strain assumption upon yielding allows $\Omega\gamma \ll 2$; therefore, the above relationship can be simplified to determine P/A by:

$$\frac{P}{A} \approx \frac{2\phi}{\alpha^2} \tag{B3}$$

Finally, the dynamic recovery Ω and mean slip distance parameter of geometrically-necessary dislocations Λ_g can be found by error minimization of the stress-strain plot. The recovery factor is first increased to match the curvature at the low-strain region of the curve. Subsequently, Λ_g is adjusted to match the high-strain stage III region of the stress-strain curve.

References

Abedrabbo, N., Pourboghrat, F. and Carsley, J., 2007. Forming of AA5182-O and AA5754-O at elevated temperatures using coupled thermo-mechanical finite element models. *International Journal of Plasticity*, *23*(5), pp.841-875.

Altintas, S., 1978. Plastic deformation of crystals: Analytical and computer simulation studies of dislocation glide [Ph. D. Thesis].

Altintas, S., 2011. Plastic deformation of crystals: analytical and computer simulation studies of dislocation glide. *Lawrence Berkeley National Laboratory*.

Anand, L., 1982. Constitutive equations for the rate-dependent deformation of metals at elevated temperatures. *Journal of engineering materials and technology*, *104*(1), pp.12-17.

Argon, A.S., 1968. Dislocation dynamics. *Materials Science and Engineering*, *3*(1), pp.24-32.

Ashby, M.F., 1970. The deformation of plastically non-homogeneous materials. *Philosophical Magazine*, *21*(170), pp.399-424.

Ayres, R.A. and Wenner, M.L., 1979. Strain and strain-rate hardening effects in punch stretching of 5182-0 aluminum at elevated temperatures. *Metallurgical Transactions A*, *10*(1), pp.41-46.

Basinski, Z.S., 1959. Thermally activated glide in face-centred cubic metals and its application to the theory of strain hardening. *Philosophical Magazine*, *4*(40), pp.393-432.

Bergström, Y. and Hallén, H., 1982. An improved dislocation model for the stress-strain behaviour of polycrystalline α-Fe. *Materials Science and Engineering*, *55*(1), pp.49-61.

Bergström, Y, 1977. Metallers Plastiska Deformation, *Royal Institute of Technology*, Stockholm.

Brahme, A.P., Inal, K., Mishra, R.K. and Saimoto, S., 2011. A new strain hardening model for rate-dependent crystal plasticity. *Computational Materials Science*, *50*(10), pp.2898-2908.

Chung, K. and Shah, K., 1992. Finite element simulation of sheet metal forming for planar anisotropic metals. *International Journal of Plasticity*, *8*(4), pp.453-476.

Clayton, J.D., 2005. Dynamic plasticity and fracture in high density polycrystals: constitutive modeling and numerical simulation. *Journal of the Mechanics and Physics of Solids*, *53*(2), pp.261-301.

Cottrell, A.H. and Stokes, R.J., 1955, December. Effects of temperature on the plastic properties of aluminium crystals. In *Proceedings of the Royal Society of London A: Mathematical, Physical and Engineering Sciences* (Vol. 233, No. 1192, pp. 17-34). The Royal Society.

Coulomb, P. and Friedel, J., 1957. Dislocations and Mechanical Properties of Crystals. *New York*.

Cyr, E.D., Mohammadi, M., Mishra, R.K. and Inal, K., 2015. A three dimensional (3D) thermo-elasto-viscoplastic constitutive model for FCC polycrystals. *International Journal of Plasticity*, *70*, pp.166-190.

Diak, B.J., Upadhyaya, K.R. and Saimoto, S., 1998. Characterization of thermodynamic response by materials testing. *Progress in materials science*, *43*(4), pp.223-363.

Elkhodary, K.I. and Bakr, M.A., 2015. Single crystal plasticity with bend–twist modes. *Journal of the Mechanics and Physics of Solids*, *79*, pp.44-66.

Ezatpour, H.R., Sabzevar, M.H., Sajjadi, S.A. and Huang, Y., 2014. Investigation of work softening mechanisms and texture in a hot deformed 6061 aluminum alloy at high temperature. *Materials Science and Engineering: A*, *606*, pp.240-247.

Foreman, A.J.E. and Makin, M.J., 1966. Dislocation movement through random arrays of obstacles. *Philosophical magazine*, *14*(131), pp.911-924.

Foreman, A.J.E. and Makin, M.J., 1967. Dislocation movement through random arrays of obstacles. *Canadian Journal of Physics*, *45*(2), pp.511-517.

Friedel, J., Dislocations, 1964. *Oxford*, *70*, pp.15-24.

Gerken, J.M. and Dawson, P.R., 2008. A crystal plasticity model that incorporates stresses and strains due to slip gradients. *Journal of the Mechanics and Physics of Solids*, *56*(4), pp.1651-1672.

Gottstein, G. ed., 2004. *Integral materials modelling*. Institute of Physics Publishing.

Gottstein, G., 2013. *Physical foundations of materials science*. Springer Science & Business Media.

Greene, D.L. and DeCicco, J., 2000. Engineering-Economic Analyses of Automotive fuel Economy Potential in the United States 1. *Annual Review of Energy and the Environment*, *25*(1), pp.477-535.

Grilli, N., Janssens, K.G. and Van Swygenhoven, H., 2015. Crystal plasticity finite element modelling of low cycle fatigue in fcc metals. *Journal of the Mechanics and Physics of Solids*, *84*, pp.424-435.

Hallén, H., 1985. A theory of dynamic recovery in FCC metals. *Materials Science and Engineering*, *72*(2), pp.119-123.

Hirth, J.P., Lothe, J., 1967. *Theory of Dislocations*. McGraw-Hill.

Inal, K., 2002. Numerical simulation of sheet metal forming processes and localized deformation phenomena for fcc polycrystals. *National Library of Canada*, University of Sherbrooke, PhD Thesis.

Inal, K., Neale, K.W. and Aboutajeddine, A., 2005. Forming limit comparisons for FCC and BCC sheets. *International Journal of Plasticity*, *21*(6), pp.1255-1266.

Jobba, M., Mishra, R.K. and Niewczas, M., 2015. Flow stress and work-hardening behaviour of Al–Mg binary alloys. *International Journal of Plasticity*, *65*, pp.43-60.

Kim, J.H., Kim, D., Barlat, F. and Lee, M.G., 2012. Crystal plasticity approach for predicting the Bauschinger effect in dual-phase steels. *Materials Science and Engineering: A*, *539*, pp.259-270.

Knezevic, M., McCabe, R.J., Lebensohn, R.A., Tomé, C.N., Liu, C., Lovato, M.L. and Mihaila, B., 2013. Integration of self-consistent polycrystal plasticity with dislocation density based hardening laws within an implicit finite element framework: application to low-symmetry metals. *Journal of the Mechanics and Physics of Solids*, *61*(10), pp.2034-2046.

Kocks, U.F., 1967. Statistical treatment of penetrable obstacles. *Canadian Journal of Physics*, *45*(2), pp.737-755.

Kocks, U.F., 1976. Laws for work-hardening and low-temperature creep. *Journal of engineering materials and technology*, *98*(1), pp.76-85.

Kocks, U.F., 2001. Realistic constitutive relations for metal plasticity. *Materials Science and Engineering: A*, *317*(1), pp.181-187.

Kocks, U.F., Argon, A.S. and Ashby, T., 1975. Kinetics of Slip. *Progress in Materials Science*, *19*.

Kocks, U.F. and Mecking, H., 2003. Physics and phenomenology of strain hardening: the FCC case. *Progress in materials science*, *48*(3), pp.171-273.

Kooiman, M., Hütter, M. and Geers, M.G.D., 2015. Microscopically derived free energy of dislocations. *Journal of the Mechanics and Physics of Solids*, *78*, pp.186-209.

Kooiman, M., Hütter, M. and Geers, M.G.D., 2016. Free energy of dislocations in a multi-slip geometry. *Journal of the Mechanics and Physics of Solids*, *88*, pp.267-273.

Kuhlmann-Wilsdorf, D., 1970. A critical test on theories of work-hardening for the case of drawn iron wire. *Metallurgical Transactions*, *1*(11), pp.3173-3179.

Li, H.Z., Wang, H.J., Liang, X.P., Liu, H.T., Liu, Y. and Zhang, X.M., 2011. Hot deformation and processing map of 2519A aluminum alloy. *Materials Science and Engineering: A*, *528*(3), pp.1548-1552.

Louat, N., 1978. On the thermal activation of dislocation motion through random point obstacles. *Acta Metallurgica*, *26*(10), pp.1597-1604.

Mecking, H., Nicklas, B., Zarubova, N. and Kocks, U.F., 1986. A “universal” temperature scale for plastic flow. *Acta Metallurgica*, *34*(3), pp.527-535.

Mianroodi, J.R., Hunter, A., Beyerlein, I.J. and Svendsen, B., 2016. Theoretical and computational comparison of models for dislocation dissociation and stacking fault/core formation in fcc crystals. *Journal of the Mechanics and Physics of Solids*.

Mohammadi, M., Brahme, A.P., Mishra, R.K. and Inal, K., 2014. Effects of post-necking hardening behavior and equivalent stress–strain curves on the accuracy of M–K based forming limit diagrams. *Computational Materials Science*, *85*, pp.316-323.

Mompiou, F., Caillard, D., Legros, M. and Mughrabi, H., 2012. In situ TEM observations of reverse dislocation motion upon unloading in tensile-deformed UFG aluminium. *Acta Materialia*, *60*(8), pp.3402-3414.

Muhammad, W., Mohammadi, M., Kang, J., Mishra, R.K. and Inal, K., 2015. An elasto-plastic constitutive model for evolving asymmetric/anisotropic hardening behavior of AZ31B and ZEK100 magnesium alloy sheets considering monotonic and reverse loading paths. *International Journal of Plasticity*, *70*, pp.30-59.

Nabarro, F.R.N., 1989. Work hardening and dynamical recovery of FCC metals in multiple glide. *Acta metallurgica*, *37*(6), pp.1521-1546.

Nabarro, F.R.N., Basinski, Z.S. and Holt, D.B., 1964. The plasticity of pure single crystals. *Advances in Physics*, *13*(50), pp.193-323.

Naka, T., Torikai, G., Hino, R. and Yoshida, F., 2001. The effects of temperature and forming speed on the forming limit diagram for type 5083 aluminum–magnesium alloy sheet. *Journal of Materials Processing Technology*, *113*(1), pp.648-653.

Nes, E., 1998. Modelling of work hardening and stress saturation in fcc metals. *Progress in Materials Science, 41*, pp.129-193

Nes, E. and Marthinsen, K., 2002. Modeling the evolution in microstructure and properties during plastic deformation of fcc-metals and alloys–an approach towards a unified model. *Materials Science and Engineering: A*, *322*(1), pp.176-193.

Niewczas, M., Jobba, M. and Mishra, R.K., 2015. Thermally activated flow of dislocations in Al–Mg binary alloys. *Acta Materialia*, *83*, pp.372-382.

Orowan, E., 1940. Problems of plastic gliding. *Proceedings of the Physical Society*, *52*(1), p.8.Park, D.Y. and Niewczas, M., 2008. Plastic deformation of Al and AA5754 between 4.2 K and 295K. *Materials Science and Engineering: A*, *491*(1), pp.88-102.

Pandey, A., Khan, A.S., Kim, E.Y., Choi, S.H. and Gnäupel-Herold, T., 2013. Experimental and numerical investigations of yield surface, texture, and deformation mechanisms in AA5754 over low to high temperatures and strain rates. *International Journal of Plasticity*, *41*, pp.165-188.

Park, D.Y. and Niewczas, M., 2008. Plastic deformation of Al and AA5754 between 4.2 K and 295K. *Materials Science and Engineering: A*, *491*(1), pp.88-102.

Peirce, D., Asaro, R.J. and Needleman, A., 1983. Material rate dependence and localized deformation in crystalline solids. *Acta metallurgica*, *31*(12), pp.1951-1976.

Popova, E., Staraselski, Y., Brahme, A., Mishra, R.K. and Inal, K., 2015. Coupled crystal plasticity–Probabilistic cellular automata approach to model dynamic recrystallization in magnesium alloys. *International Journal of Plasticity*, *66*, pp.85-102.

Porter, D.A., Easterling, K.E. and Sherif, M., 2009. *Phase Transformations in Metals and Alloys, (Revised Reprint)*. CRC press.Rodriguez, P., 1996. Sixty years of dislocations. *Bulletin of Materials Science*, *19*(6), pp.857-872.

Roters, F., Eisenlohr, P., Hantcherli, L., Tjahjanto, D.D., Bieler, T.R. and Raabe, D., 2010. Overview of constitutive laws, kinematics, homogenization and multiscale methods in crystal plasticity finite-element modeling: Theory, experiments, applications. *Acta Materialia*, *58*(4), pp.1152-1211.

Roters, F., Raabe, D. and Gottstein, G., 2000. Work hardening in heterogeneous alloys—a microstructural approach based on three internal state variables. *Acta materialia*, *48*(17), pp.4181-4189.

Robinson, J.M. and Shaw, M.P., 1994. Microstructural and mechanical influences on dynamic strain aging phenomena. *International Materials Reviews*, *39*(3), pp.113-122.

Rossiter, J., Brahme, A., Inal, K. and Mishra, R., 2013. Numerical analyses of surface roughness during bending of FCC single crystals and polycrystals. *International Journal of Plasticity*, *46*, pp.82-93.

Saimoto, S., 2006. Dynamic dislocation–defect analysis. *Philosophical Magazine*, *86*(27), pp.4213-4233.

Saimoto, S. and Van Houtte, P., 2011. Constitutive relation based on Taylor slip analysis to replicate work-hardening evolution. *Acta Materialia*, *59*(2), pp.602-612.

Schafler, E., Simon, K., Bernstorff, S., Hanák, P., Tichy, G., Ungár, T. and Zehetbauer, M.J., 2005. A second-order phase-transformation of the dislocation structure during plastic deformation determined by in situ synchrotron X-ray diffraction. *Acta materialia*, *53*(2), pp.315-322.

Schoeck, G. and Seeger, A., 1955. Report on the Conference of Defects in Crystalline Solids, Bristol, 1954. *London: The Physical Society*.

Seeger, A., Berner, R., Wolf, H., 1959. *Z. Physic*, *155*, pp.247

Sevillano, J.G., Van Houtte, P. and Aernoudt, E., 1980. Large strain work hardening and textures. *Progress in Materials Science*, *25*(2-4), pp.69-134.

Staker, M.R. and Holt, D.L., 1972. The dislocation cell size and dislocation density in copper deformed at temperatures between 25 and 700 C. *Acta Metallurgica*, *20*(4), pp.569-579.

Svendsen, B., 2002. Continuum thermodynamic models for crystal plasticity including the effects of geometrically-necessary dislocations. *Journal of the Mechanics and Physics of Solids*, *50*(6), pp.1297-1329.

Taylor, G.I., 1934. The mechanism of plastic deformation of crystals. Part I. Theoretical. *Proceedings of the Royal Society of London. Series A, Containing Papers of a Mathematical and Physical Character*, *145*(855), pp.362-387.

Takata, K., Ohwue, T., Saga, M. and Kikuchi, M., 2000. Formability of Al-Mg alloy at warm temperature. In *Materials science forum* (Vol. 331, pp. 631-636). Trans Tech Publications.

Terentyev, D., Xiao, X., Dubinko, A., Bakaeva, A. and Duan, H., 2015. Dislocation-mediated strain hardening in tungsten: Thermo-mechanical plasticity theory and experimental validation. *Journal of the Mechanics and Physics of Solids*, *85*, pp.1-15.

Thompson, A.W., 1977. Substructure strengthening mechanisms. *Metallurgical Transactions A*, *8*(6), pp.833-842.

Van den Boogaard, A.H., Bolt, P.J. and Werkhoven, R.J., 2001. Aluminum sheet forming at elevated temperatures. *Simulation of Materials Processing: Theory, Method and Applications*, pp.819-824.

Varshni, Y.P., 1970. Temperature dependence of the elastic constants. *Physical Review B*, *2*(10), p.3952.

Wu, P.D., Neale, K.W. and Van der Giessen, E., 1997, September. On crystal plasticity FLD analysis. In *Proceedings of the Royal Society of London A: Mathematical, Physical and Engineering Sciences* (Vol. 453, No. 1964, pp. 1831-1848). The Royal Society.

Zhang, H., Lin, G.Y., Peng, D.S., Yang, L.B. and Lin, Q.Q., 2004. Dynamic and static softening behaviors of aluminum alloys during multistage hot deformation. *Journal of materials processing technology*, *148*(2), pp.245-249.

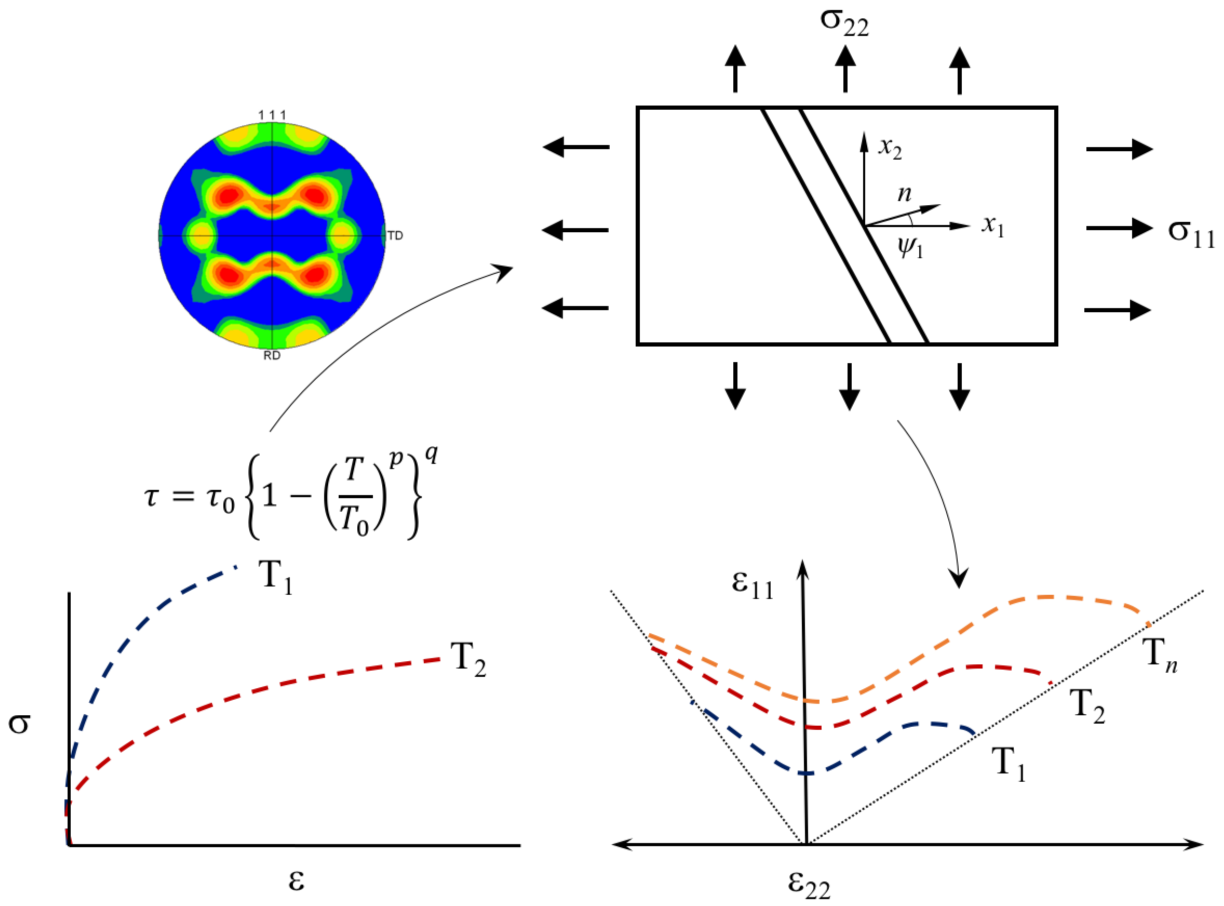

111
TD
RD
σ_{22}
x_2
n
x_1
ψ_1
σ_{11}
$\tau = \tau_0 \left\{1 - \left(\frac{T}{T_0}\right)^p\right\}^q$
T_1
T_2
σ
ε
ε_{11}
T_n
T_2
T_1
ε_{22}

Graphical Abstract